Journal of JSCE, Vol. 1, 194-213, 2013

THREE-DIMENSIONAL MODELING OF HYDRODYNAMICS AND DISSOLVED OXYGEN TRANSPORT IN TONE RIVER ESTUARY

Xiaofei XU[1], Tadaharu ISHIKAWA[2] and Takashi NAKAMURA[3]

[1] School of Chemical Machinery, Dalian University of Technology
(No.2 Linggong Road, Gangjingzi District, Dalian City, Liaoning Province, 116024, China)
E-mail: xiaofei.xu@yahoo.com.cn
[2]Fellow Member of JSCE, Professor, Dept. Environmental Science & Technology, Tokyo Institute of Technology
(Nagatsuta 4259, Midori-ku, Yokohama, 226-8502, Japan)
E-mail: ishikawa.t.ai@m.titech.ac.jp
[3]Member of JSCE, Associate Professor, Dept. Environmental Science & Technology, Tokyo Institute of Technology
(Nagatsuta 4259, Midori-ku, Yokohama, 226-8502, Japan)
E-mail: nakamura.t.ah@m.titech.ac.jp

A three-dimensional hydrodynamic model for simulating estuarine dynamics has been developed. The model, called CIP-Soroban flow solver, has been specifically designed for reproducing the current and salinity fields in density-stratified water bodies with a free surface. It is based on the Constrained Interpolation Profile (CIP) scheme and the Soroban computational grid system. Simulations of the time-dependent current and salinity fields of the Tone River Estuary have been performed using this model. Two periods are used to examine the predictive capability of the model. The first was in August 1997, which produced extensive field data related to vertical profiles of salinity, which showed evident changes in salinity intrusion processes between spring and neap tides; and the second in August 2001, which produced sufficient data associated with continuous measurements of vertical profiles of velocity, which showed characteristic residual flows averaged over ten tidal cycles. The model is examined in detail to reveal its inherent capability of simulating the dynamic behavior of density flow in the Tone River Estuary. In these two periods, the measured salinity and velocity data are reproduced well by the 3-D model. After investigating the capability of the hydrodynamic model, the dissolved oxygen (DO) transport model is incorporated into the hydrodynamic model to study the role of density stratification and residence time of seawater at the onset and development of hypoxia. The results of a long-term simulation of 100 days show good agreement with the field data.

Key Words: *3-D model, CIP-Soroban scheme, Tone River Estuary, estuarine flow, DO transport*

1. INTRODUCTION

Estuaries, the transition zones between river environments and ocean environments, are valuable natural resources. The exhaustible nature of estuarine resources requires that they be afforded a high level of environmental protection. Environmental impact assessments usually depend on a good understanding of the physical processes of water circulation and mixing. However, these physical processes in estuarine environments are often very complicated because of the presence of the salinity gradient in both the horizontal and vertical directions. The horizontal salinity gradient is the key driving force for estuarine circulation, which in turn plays a key role in maintaining salinity stratification[1)]. The vertical salinity gradient, which is a major reason for density stratification, has significant effects on the vertical mixing. The spatial distributions of salinity are also influential in the distribution and transport of dissolved oxygen (DO) and suspended sediment. Hypoxia can often be generated in the saline bottom water layer at the head of the salt wedge because the vertical density stratification reduces the vertical mixing between the oxygen-rich surface water layer and the oxygen-deficient bottom water layer[2)]. Furthermore, when suspended sediment, to which organic matter and nutrients attach, meets the saline water, it tends to deposit after flocculation, which results in deterioration of bottom sediment[3)]. Therefore, effective utili-

zation and management of estuaries work on the premise that the physical processes of water circulation and mixing closely related to the salinity gradient are fully understood.

Numerical modeling is an effective way of studying the circulation and mixing processes in estuaries and can compensate for the spatial and temporal limitations of field measurements. In the early numerical models, because of the high cost of computation, simplification of governing equations by a laterally-averaged approach[4)-6)] has been widely used in stratified water bodies. This approach supposes that the detailed flow in the transverse direction is relatively unimportant, and the effect of vertical velocity and salinity variation cannot be neglected. However, when the lateral flows driven by the balance of Coriolis acceleration, flow curvature and cross-channel baroclinic pressure gradients[1)] cannot be ignored, a 3-D model may be required.

Meanwhile, in recent years, improvements in computer performance and advances in numerical methods have also stimulated an increase in the development of 3-D models. One of the major differences among the numerical models is the type of vertical coordinate system. The common way to discretize the water depth is either with an untransformed z coordinate (z-level) system or a transformed coordinate (σ-level) system. Both have their drawbacks. The biggest problem for the z-level model with horizontal layers is that it cannot fit the topography properly[7)]. Although the σ-level model does not have the topography-fitting problem and it can map the surface and bottom into horizontal coordinate surfaces, the σ transformation can lead to severe numerical errors in regions of rapidly changing depth, which is common in estuaries[8)]. Meanwhile, to reduce the numerical diffusion errors around the fresh-saline water interface, the σ coordinate model needs to employ a large number of vertical grid layers, which often leads to "over-resolution" in the shallow regions and unnecessarily increases computational costs[9)].

To overcome the shortages of the two above-mentioned conventional grid systems but also draw upon the best features of each, a new 3-D numerical model, called CIP-Soroban estuary solver, is developed in this work. In the solver, to suppress numerical diffusion errors, advection terms are solved by the Constrained Interpolation Profile (CIP) scheme with third-order accuracy; and to achieve a precise description of fresh-saline water interface, the water depth is discretized with a new adoptive grid system called the Soroban grid system. In the Soroban grid system, grid points can be moved freely and gathered around an arbitrary region. Thus the sharp discontinuity at the fresh-saline water interface can be represented well by gathering more grid points around it. As a result of this excellent numerical feature, the proposed numerical model is expected to simulate the estuarine dynamics even if a relatively coarse mesh is employed. Furthermore, since spatial interpolations and approximations of spatial derivatives are estimated in the Cartesian coordinate system in the CIP-Soroban scheme, it is expected that this scheme can avoid the severe artificial numerical error present in the σ-level model.

In the following sections, the basic idea of the CIP-Soroban scheme is introduced and the governing equations and numerical procedures are described. Next, the present model is applied to the Tone River Estuary with realistic topography and controlled by tides, winds and river discharges. Through comparisons of the computed results with the field data, the capability of the 3-D model to reproduce the salinity field and flow structure is studied. Furthermore, to reveal the unique features of the 3-D model, the 3-D computed results are compared with the results of a laterally-averaged 2-D model which is also based on the CIP-Soroban scheme and was developed by Nakamura et al.[6)]. Finally, the DO transport model is incorporated into the hydrodynamic model to study the role of the salinity stratification and residence time of seawater at the onset and development of hypoxia.

2. DESCRIPTION OF THE MODEL

The essential feature of this hydrodynamic model is the application of the CIP-Soroban scheme to model the flow and mixing processes in estuarine environments. The CIP-Soroban scheme is a combination of the CIP technique developed by Yabe et al.[10)-12)] for solving hyperbolic problems and the Soroban grid system, an adaptive grid system[13)-14)] that allows the CIP scheme to be applied to it. In this section, the characteristics of the CIP scheme and Soroban grid system are described, and then the governing equations and the numerical procedure of the model are introduced.

(1) Basic concept of the CIP scheme

The CIP scheme is a kind of semi-Lagrangian scheme which has been developed to solve advection equations with few numerical errors. It is characterized by employing the cubic polynomial as an interpolation function to achieve third-order accuracy in space. To show the basic concept of the CIP scheme, here we briefly describe the numerical procedures of the CIP scheme by using a 1-D advection equation:

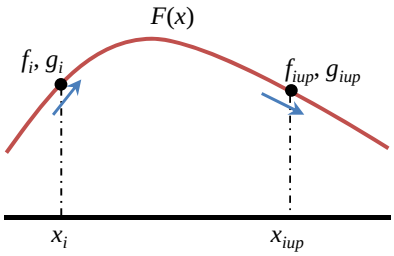

Fig. 1 Schematic diagram of CIP interpolation.

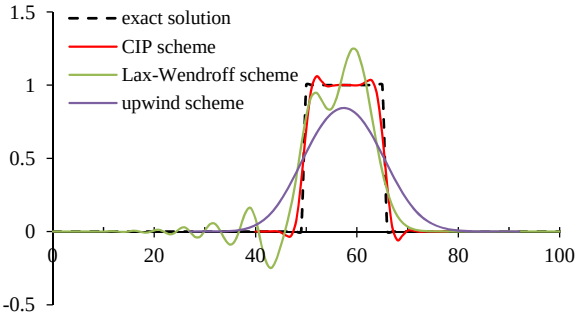

Fig. 2 Square wave propagation tests by several schemes.

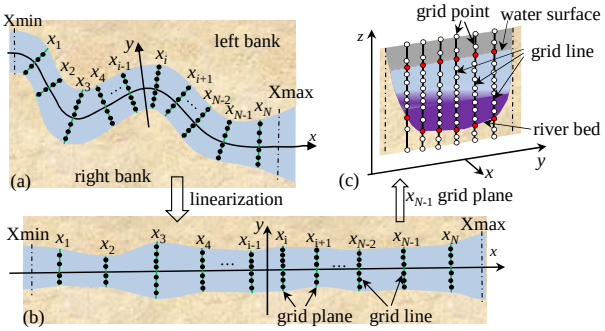

Fig. 3 Grid configuration: (a) and (b) linearizing the river channel along the *x*-axis; (c) arrangement of grid lines and points on a grid plane.

$$\frac{\partial f}{\partial t} + u\frac{\partial f}{\partial x} = 0 \tag{1}$$

Even if u is a function of time t and space x, we can locally use the solution as follows:

$$f(x_i, t+\Delta t) = f(x_i - u_i\Delta t, t) \tag{2}$$

where x_i and u_i are the grid point and the velocity at x_i, respectively. According to equation (2), the time evolution of f can be calculated by interpolating the value of $f(x_i\text{-}u_i\Delta t, t)$. In the CIP scheme, in addition to the value of f, its spatial derivative $\partial f / \partial x$ ($\equiv g$) is also introduced on each grid point and the time development of g is solved. If we differentiate equation (1) with respect to x, we obtain

$$\frac{\partial g}{\partial t} + u\frac{\partial g}{\partial x} = -\frac{\partial u}{\partial x}g \tag{3}$$

Equation (3) is merely an advection equation with the velocity u the same as in Equation (1). Therefore, g can also be calculated the same way as f. By using equations (1) and (3), we can trace the time evolution of f and g[10].

The spatial profile between the two neighboring points is interpolated by a cubic polynomial $F(x) = ax^3 + bx^2 + cx + d$ (**Fig. 1**). The coefficients a, b, c and d can be determined explicitly according to the value of f and its spatial derivative g on each grid point. Thus, the value and spatial derivative at time step $n+1$ can be obtained by transporting the profile by $u_i\Delta t$ as follows:

$$f_i^{n+1} = F(x_i - u_i\Delta t) = a_i\xi^3 + b_i\xi^2 + g_i^n\xi + f_i^n \tag{4a}$$

$$g_i^{n+1} = \frac{dF}{dx}(x_i - u_i\Delta t) = 3a_i\xi^2 + 2b_i\xi + g_i^n \tag{4b}$$

$$\begin{aligned} a_i &= \frac{g_i + g_{iup}}{D^2} + \frac{2(f_i - f_{iup})}{D^3} \\ b_i &= \frac{3(f_{iup} - f_i)}{D^2} - \frac{2g_i + g_{iup}}{D} \end{aligned} \tag{5}$$

where $\xi \equiv -u_i\Delta t$. The variables *iup* and D represent the upstream grid point and the distance from i to *iup*:

$$(iup, D) = \begin{cases} (i\text{-}1, -\Delta x) & \text{for } u>0 \\ (i+1, \Delta x) & \text{otherwise} \end{cases} \tag{6}$$

Figure 2 shows the square wave propagation test results from several schemes. The CIP scheme is compared with the first-order upwind scheme and second-order Lax-Wendroff scheme. The total computational domain is $0< x <100$ and the mesh interval is 1. The Courant-Friedrich-Lewy (CFL) number is 0.2 and advection velocity is 0.2. The results in **Fig. 2** are obtained after 200 time steps. From these results, the CIP scheme shows a good shape-conserving result with low dispersion and dissipation errors in contrast to the upwind and Lax-Wendroff schemes.

(2) Grid system

a) Soroban grid system

The Soroban grid system is named after the Japanese abacus "Soroban". It consists of grid planes, straight lines and grid points placed along the lines like in an abacus. The length of each line and the number of grid points on each line can be different depending on the required resolution. The Soroban grid can readily incorporate local mesh refinement, which means the gathering of grid points can be easily preformed.

Since the Soroban grid system was originally proposed for the Cartesian coordinate system[13], it is difficult to apply it directly to meandering rivers. Therefore, we employ the deepest line of the channel as the x-axis (**Fig. 3a**) and linearize the river channel along the x-axis (**Fig. 3b**). Effects of meandering are taken into account by additionally introducing centrifugal terms in the momentum equations depending on the radius of curvature of the channel. However, since the difference in distance along the inner and outer banks in the along-channel direction resulting from the river meandering is not considered, the

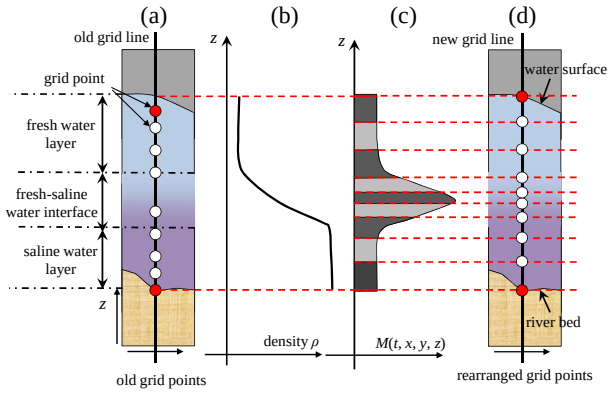

Fig. 4 Grid points concentrated around the fresh-saline water interface according to monitoring function *M*.

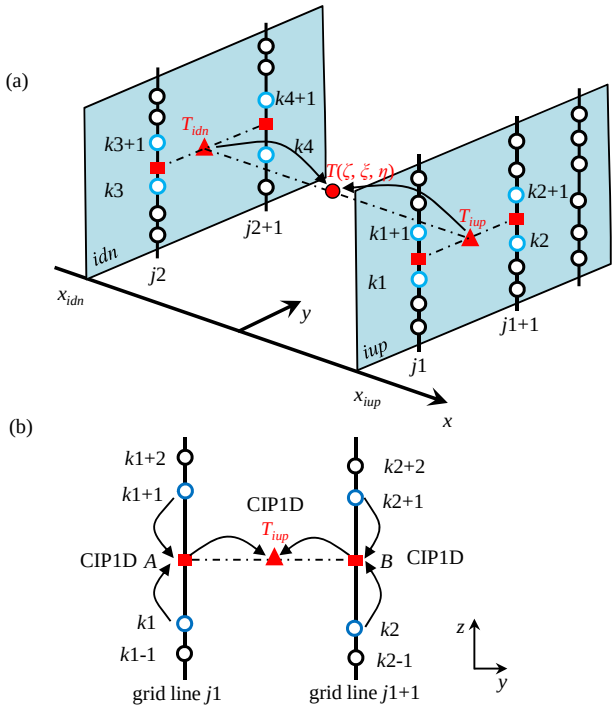

Fig. 5 Schematic of advection calculation in the Soroban grid: (a) three-dimensional Soroban grid; (b) grid lines and grid points on grid plane *iup*.

applicability of the present model to the river channel with large meandering needs further study. As shown in **Fig. 3b** and **c**, the *y*-axis is set to be orthogonal to the *x*-axis and increasing from right bank to left bank, and the *z*-axis is increasing vertically upwards.

There are three steps to discretize the computational domain using the Soroban grid technique. Firstly, we discretize the computational domain using grid planes which are perpendicular to the *x*-axis (**Fig. 3b**). Then, as shown in **Fig. 3c**, some parallel grid lines are aligned to discretize the planes and some grid points are distributed on the lines, just as an abacus has moveable counters strung on parallel rods. In contrast to other adaptive grid systems, the structured configuration of plane, line and point makes the finding of neighboring points very easy and fast[13].

b) Adaptive remeshing on the Soroban grid

Like the moveable counters strung on rods in the abacus, grid points can be rearranged along the grid lines at each time step. This can improve spatial accuracy and reduce numerical diffusion errors by concentrating the grid points around the fresh-saline water interface.

The remeshing process is carried out individually on each grid line. A schematic view of the remeshing process on a line is shown in **Fig. 4**. Note that positions of the fresh-saline water interface and water surface are changing at each time step. So in order to concentrate the grid points around the fresh-saline water interface, the interface should be detected first according to the following monitoring function *M*:

$$M(x_i, y_{ij}, z_{ijk}) = \sqrt{1+\alpha(\partial\rho/\partial z)} \qquad (7)$$

where x_i, y_{ij}, z_{ijk} = location of each grid point; α = scaling coefficient, which is a positive constant; and ρ = density. Actually, as shown in **Fig. 4b** and **c**, the monitoring function *M* is larger around the fresh-saline water interface because the density gradients are relatively large in this region. Then, the estimated profile of *M* is divided into several equal partitions (**Fig. 4c**) and new vertical positions of the grid points are determined by the boundaries of each partition (**Fig. 4d**). Based on the above process, more grid points can be gathered around the fresh-saline water interface. Furthermore, the kinematic and dynamic boundary conditions can be easily imposed by placing a grid point on the water surface and river bed.

c) Application of CIP to the Soroban grid

'Type-M' CIP[13] is a dimensional splitting scheme, which makes the CIP interpolation easy to apply on the Soroban grid to calculate the advection terms. CIP interpolation is performed in the Cartesian coordinate system. The grid lines and points on two neighboring planes, shown in **Fig. 5**, are considered. Let (*i*, *j*, *k*) be the grid point of interest. As shown in **Fig. 5a**, if the upstream departure point *T* is given as $(\zeta, \xi, \eta) = (x_i - u_{i,j,k}\Delta t, y_{i,j} - v_{i,j,k}\Delta t, z_{i,j,k} - w_{i,j,k}\Delta t)$, first, one pair of planes *iup* and *idn* is searched to satisfy $x_{idn} < \zeta < x_{iup}$. Next two pairs of grid lines are searched on the grid plane *idn* and *iup* to satisfy $y_{iup,j1} < \xi < y_{iup,j1+1}$ and $y_{idn,j2} < \xi < y_{idn,j2+1}$. Then four pairs of grid points are searched along the grid line *j*1, *j*1+1, *j*2 and *j*2+1 to satisfy $z_{iup,j1,k1} < \eta < z_{iup,j1,k1+1}$ and $z_{iup,j1+1,k2} < \eta < z_{iup,j1+1,k2+1}$, $z_{idn,j2,k3} < \eta < z_{idn,j2,k3+1}$ and $z_{idn,j2+1,k4} < \eta < z_{idn,j2+1,k4+1}$. Finally, the interpolations are performed by using the eight grid points (*iup*, *j*1, *k*1), (*iup*, *j*1, *k*1+1), (*iup*, *j*1+1, *k*2), (*iup*, *j*1+1,*k*2+1), (*idn*, *j*2, *k*3), (*idn*, *j*2, *k*3+1), (*idn*, *j*2+1, *k*4) and (*idn*, *j*2+1, *k*4+1) to determine the value at *T*.

To obtain the value at *T*, first of all, the value at T_{iup} and T_{idn} on the grid planes *iup* and *idn* should be

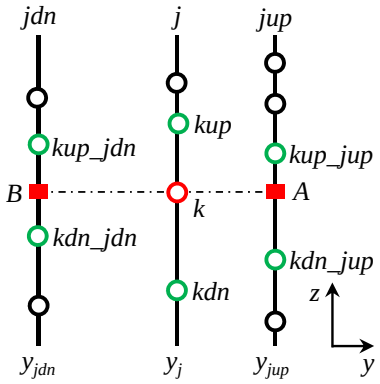

Fig. 6 Finite difference approximations in the Soroban grid.

determined. On grid plane *iup*, as shown in **Fig. 5b**, one-dimensional CIP is employed to calculate the value at *A* and *B* along the straight line *j*1 and *j*1+1, respectively. Then one-dimensional CIP is used again to calculate the value at point T_{iup} along the horizontal line connecting *A* and *B*. The same procedure is repeated for calculating the value at T_{idn} on grid plane *idn*. Lastly, one-dimensional CIP is used to calculate the value at point *T* along the horizontal line connecting T_{iup} and T_{idn} (**Fig. 5a**). Thus the value at (*i*, *j*, *k*) at the next time step after advection are given as the value at *T*.

d) Finite difference approximation in the Soroban grid

The non-advection terms in the model, such as diffusion terms and turbulence production terms are solved by the finite difference method. Here we take the two-dimensional mesh in the *y*-*z* plane as an example to describe the process of deriving the finite difference approximation in the Soroban grid in brief (**Fig. 6**). Let (*j*, *k*) be the grid point of interest. If the coordinates at (*j*, *k*) are given as (y_j, z_k), one pair of points satisfying $z_{kup} < z_k < z_{kdn}$ is searched along the straight line *j*. After that, the same procedure is repeated along the nearest upstream line *jup* and downstream line *jdn*, respectively. These six points are used to derive the spatial derivatives at (*j*, *k*).

The approximation of the first and second derivatives of *y* at (*j*, *k*) is calculated along the horizontal line connecting *A* and *B* by the following equations:

$$\left(\frac{\partial f}{\partial y}\right)_{j,k} = \frac{f_A - f_B}{y_{jup} - y_{jdn}} \tag{8a}$$

$$\left(\frac{\partial^2 f}{\partial y^2}\right)_{j,k} = \frac{1}{(y_{jup} - y_j)(y_{jup} - y_{jdn})/2} f_A - \left(\frac{1}{(y_{jup} - y_j)(y_{jup} - y_{jdn})/2} + \frac{1}{(y_j - y_{jdn})(y_{jup} - y_{jdn})/2}\right) f_k + \frac{1}{(y_j - y_{jdn})(y_{jup} - y_{jdn})/2} f_B \tag{8b}$$

where *f* = physical quantity at the grid point. The physical quantities at *A* and *B* are estimated by linear interpolation along lines *jup* and *jdn*, respectively. As described above, approximation of horizontal derivatives are evaluated in the Cartesian coordinate system. Slordal[15] and Stelling and van Kester[16] proposed similar approaches to estimate the horizontal derivatives as a modification of the σ-level model, and they demonstrated that this approximation in the Cartesian coordinate system can suppress the artificial numerical errors in regions with rapidly changing depth.

The approximation of the first and second derivatives of *z* at (*j*, *k*) is calculated along the line *j* by the following equations:

$$\left(\frac{\partial f}{\partial z}\right)_{j,k} = \frac{f_{kup} - f_{kdn}}{z_{kup} - z_{kdn}} \tag{9a}$$

$$\left(\frac{\partial^2 f}{\partial z^2}\right)_{j,k} = \frac{1}{(z_{kup} - z_k)(z_{kup} - z_{kdn})/2} f_{kup} - \left(\frac{1}{(z_{kup} - z_k)(z_{kup} - z_{kdn})/2} + \frac{1}{(z_k - z_{kdn})(z_{kup} - z_{kdn})/2}\right) f_k + \frac{1}{(z_k - z_{kdn})(z_{kup} - z_{kdn})/2} f_{kdn} \tag{9b}$$

(3) Governing equations

The three-dimensional CIP-Soroban model is based on the three-dimensional Reynolds-averaged Navier-Stocks equations and k - ε turbulence closure equations for incompressible flow with free surface. Time-dependent velocities, turbulence quantities and salinity can be computed by the following equations:

$$\frac{\partial u}{\partial x} + \frac{\partial v}{\partial y} + \frac{\partial w}{\partial z} = 0 \tag{10}$$

$$\frac{Du}{Dt} = -\frac{1}{\rho}\frac{\partial p}{\partial x} + \frac{uv}{R} + \frac{\tau_x}{\rho} + fv + \frac{\partial}{\partial x}\left(K_H \frac{\partial u}{\partial x}\right) + \frac{\partial}{\partial y}\left(K_H \frac{\partial u}{\partial y}\right) + \frac{\partial}{\partial z}\left(K_V \frac{\partial u}{\partial z}\right) \tag{11}$$

$$\frac{Dv}{Dt} = -\frac{1}{\rho}\frac{\partial p}{\partial y} - \frac{u^2}{R} + \frac{\tau_y}{\rho} - fu + \frac{\partial}{\partial x}\left(K_H \frac{\partial v}{\partial x}\right) + \frac{\partial}{\partial y}\left(K_H \frac{\partial v}{\partial y}\right) + \frac{\partial}{\partial z}\left(K_V \frac{\partial v}{\partial z}\right) \tag{12}$$

$$\frac{Dw}{Dt} = -\frac{1}{\rho}\frac{\partial p}{\partial z} + \frac{\tau_z}{\rho} - g + \frac{\partial}{\partial x}\left(K_H \frac{\partial w}{\partial x}\right) + \frac{\partial}{\partial y}\left(K_H \frac{\partial w}{\partial y}\right) + \frac{\partial}{\partial z}\left(K_V \frac{\partial w}{\partial z}\right) \tag{13}$$

$$\frac{Dk}{Dt} = P_k - \varepsilon + G_k + \frac{\partial}{\partial x}\left(\frac{K_H}{\sigma_k}\frac{\partial k}{\partial x}\right) + \frac{\partial}{\partial y}\left(\frac{K_H}{\sigma_k}\frac{\partial k}{\partial y}\right) + \frac{\partial}{\partial z}\left(\frac{K_V}{\sigma_k}\frac{\partial k}{\partial z}\right) \quad (14)$$

$$\frac{D\varepsilon}{Dt} = \left(c_1 P_k - c_2\varepsilon\right)\frac{\varepsilon}{k} + c_1\left(1-c_3\right)\frac{\varepsilon}{k}G_k + \frac{\partial}{\partial x}\left(\frac{K_H}{\sigma_\varepsilon}\frac{\partial \varepsilon}{\partial x}\right) + \frac{\partial}{\partial y}\left(\frac{K_H}{\sigma_\varepsilon}\frac{\partial \varepsilon}{\partial y}\right) + \frac{\partial}{\partial z}\left(\frac{K_V}{\sigma_\varepsilon}\frac{\partial \varepsilon}{\partial z}\right) \quad (15)$$

$$\frac{DS}{Dt} = \frac{\partial}{\partial x}\left(D_{H,S}\frac{\partial S}{\partial x}\right) + \frac{\partial}{\partial y}\left(D_{H,S}\frac{\partial S}{\partial y}\right) + \frac{\partial}{\partial z}\left(D_{V.S}\frac{\partial S}{\partial z}\right) \quad (16)$$

$$\frac{D}{Dt} = \frac{\partial}{\partial t} + u\frac{\partial}{\partial x} + v\frac{\partial}{\partial y} + w\frac{\partial}{\partial z} \quad (17)$$

$$P_k = K_V\left\{\left(\frac{\partial u}{\partial z}\right)^2 + \left(\frac{\partial v}{\partial z}\right)^2\right\} \quad (18)$$

$$G_k = \frac{g}{\rho}\frac{\upsilon_t}{\sigma_s}\frac{\partial \rho}{\partial z} \quad (19)$$

$$K_H = C_s^2 \Delta x \Delta y \sqrt{\left(\frac{\partial u}{\partial x}\right)^2 + \left(\frac{\partial v}{\partial y}\right)^2 + \frac{1}{2}\left(\frac{\partial u}{\partial y} + \frac{\partial v}{\partial x}\right)^2} \quad (20)$$

$$K_V = \upsilon_{mol} + \upsilon_t = \upsilon_{mol} + c_\mu \frac{k^2}{\varepsilon} \quad (21)$$

$$D_{H,S} = \frac{K_H}{\sigma_s},\ D_{V,S} = \frac{K_V}{\sigma_s} \quad (22)$$

where t = time; x, y, z = longitudinal, transverse and vertical spatial coordinates, respectively; u, v, w = velocity components in the x, y and z directions, respectively; p = pressure; ρ = water density, which is calculated from salinity based on a UNESCO empirical formula[17] at a constant temperature; τ_x, τ_y ,τ_z = total effects of shear stresses at the water surface, river bed and lateral bank in x, y and z directions, respectively, which are treated as boundary conditions; R = radius of curvature of the river channel; f = Coriolis parameter; k = turbulence kinetic energy; ε = dissipation rate of turbulence kinetic energy; P_k = generation of turbulence kinetic energy term due to vertical velocity gradients; G_k = turbulence production/destruction term, which is caused by buoyancy; K_H = horizontal diffusivity of momentum, which is calculated using the Smagorinsky subgrid scale scheme[18]; C_s = Smagorinsky constant (= 0.1); Δx, Δy = grid spacing in x and y directions, respectively; υ_{mol} = molecular viscosity of water; υ_t = vertical eddy viscosity; K_V = vertical diffusivity of momentum which consists of molecular viscosity and vertical eddy viscosity; and $D_{H,S}$, $D_{V,S}$ = diffusion coefficients of salinity in horizontal and vertical directions, respectively. The turbulence model constants are c_1 = 1.44, c_2 = 1.92, c_3 = 1.0, c_μ = 0.09, σ_k = 1.0, σ_ε = 1.3 and σ_s = 0.8.

In addition to velocities, turbulence quantities and salinity, time development of free surface elevation $h(t, x, y)$ is computed according to the following equation:

$$\frac{\partial h}{\partial t} + \frac{\partial m}{\partial x} + \frac{\partial n}{\partial y} = 0 \quad (23a)$$

where m, n = line flow rate in x and y directions, respectively. Line flow rates m and n can be derived by the following equations:

$$m(t,x,y) = \int_{b(x,y)}^{h(t_n,x,y)} u dz,\quad n(t,x,y) = \int_{b(x,y)}^{h(t_n,x,y)} v dz \quad (23b)$$

where $b(x, y)$ = river bed elevation.

The governing equations are solved by supplementing the following boundary conditions at the water surface and the river bed:

(a) Dynamic boundary condition (water surface)

$$p(t,x,y,h(t,x,y)) = 0 \quad (24a)$$

(b) Kinematic boundary condition (river bed)

$$u_n = -\frac{\partial b(x,y)}{\partial x}u_b - \frac{\partial b(x,y)}{\partial y}v_b + w_b = 0 \quad (24b)$$

where u_n = velocity components normal to the river bed and (u_b, v_b, w_b) = velocity components at the river bed in the x, y and z directions, respectively.

(4) Numerical methods

Based on the time-splitting method[6),12),13)], the governing equations are split into a series of intermediate steps: (1) advection step, (2) Soroban remeshing step, (3) turbulence step, (4) diffusion step, (5) other sources step and (6) pressure correction step. Each intermediate step is solved sequentially with the intermediate results calculated in the preceding step by using appropriate numerical methods.

Step 1: Advection step

In the first step, the advection terms of momentum equations, k and ε equations, and the salinity transport equation are calculated by applying the 'Type-M' CIP:

$$\frac{\partial u}{\partial t} + u\frac{\partial u}{\partial x} + v\frac{\partial u}{\partial y} + w\frac{\partial u}{\partial z} = 0 \quad (25a)$$

$$\frac{\partial v}{\partial t} + u\frac{\partial v}{\partial x} + v\frac{\partial v}{\partial y} + w\frac{\partial v}{\partial z} = 0 \quad (25b)$$

$$\frac{\partial w}{\partial t} + u\frac{\partial w}{\partial x} + v\frac{\partial w}{\partial y} + w\frac{\partial w}{\partial z} = 0 \quad (25c)$$

$$\frac{\partial k}{\partial t} + u\frac{\partial k}{\partial x} + v\frac{\partial k}{\partial y} + w\frac{\partial k}{\partial z} = 0 \quad (25d)$$

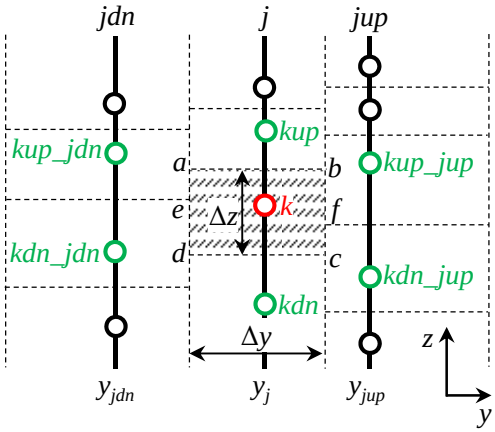

Fig.7 Finite volume approach in the Soroban grid.

$$\frac{\partial \varepsilon}{\partial t}+u\frac{\partial \varepsilon}{\partial x}+v\frac{\partial \varepsilon}{\partial y}+w\frac{\partial \varepsilon}{\partial z}=0 \tag{25e}$$

$$\frac{\partial S}{\partial t}+u\frac{\partial S}{\partial x}+v\frac{\partial S}{\partial y}+w\frac{\partial S}{\partial z}=0 \tag{25f}$$

In addition to the calculation of the above equations, the following water surface propagation equation is also solved implicitly in this step:

$$\frac{\partial h}{\partial t}+\frac{\partial m}{\partial x}+\frac{\partial n}{\partial y}=0 \tag{26}$$

Step 2: Soroban remeshing step

After the calculations in step 1, because the spatial distribution of salinity and the position of the water surface are changed, adaptive remeshing needs to be performed to capture the water surface and concentrate grid points around the fresh-saline water interface. Therefore, in step 2, a grid point is relocated onto the water surface first, and then the rest of the grid points along the grid lines are rearranged to track the fresh-saline water interface according to monitoring function M (equation 7). After the remeshing, all of the physical quantities on each newly remeshed grid point are estimated by applying the one-dimensional CIP interpolation based on values on the old grid points.

Step 3: Turbulence step

In this step, the generation of k and ε due to the turbulence production term P_k and buoyancy term G_k is calculated by applying the first-order Euler explicit scheme:

$$\frac{\partial k}{\partial t}=P_k+G_k-\varepsilon \tag{27a}$$

$$\frac{\partial \varepsilon}{\partial t}=c_1\frac{\varepsilon}{k}P_k+c_1(1-c_3)\frac{\varepsilon}{k}G_k-c_2\frac{\varepsilon^2}{k} \tag{27b}$$

Here P_k and G_k are estimated through the finite difference approximation in the Soroban grid.

Step 4: Diffusion step

In step 4, both the horizontal and vertical diffusion terms of momentum equations, k and ε equations, and the salinity transport equation are calculated.

$$\frac{\partial u}{\partial t}=\frac{\partial}{\partial x}\left(K_H\frac{\partial u}{\partial x}\right)+\frac{\partial}{\partial y}\left(K_H\frac{\partial u}{\partial y}\right)+\frac{\partial}{\partial z}\left(K_V\frac{\partial u}{\partial z}\right) \tag{28a}$$

$$\frac{\partial v}{\partial t}=\frac{\partial}{\partial x}\left(K_H\frac{\partial v}{\partial x}\right)+\frac{\partial}{\partial y}\left(K_H\frac{\partial v}{\partial y}\right)+\frac{\partial}{\partial z}\left(K_V\frac{\partial v}{\partial z}\right) \tag{28b}$$

$$\frac{\partial w}{\partial t}=\frac{\partial}{\partial x}\left(K_H\frac{\partial w}{\partial x}\right)+\frac{\partial}{\partial y}\left(K_H\frac{\partial w}{\partial y}\right)+\frac{\partial}{\partial z}\left(K_V\frac{\partial w}{\partial z}\right) \tag{28c}$$

$$\frac{\partial k}{\partial t}=\frac{\partial}{\partial x}\left(\frac{K_H}{\sigma_k}\frac{\partial k}{\partial x}\right)+\frac{\partial}{\partial y}\left(\frac{K_H}{\sigma_k}\frac{\partial k}{\partial y}\right)+\frac{\partial}{\partial z}\left(\frac{K_V}{\sigma_k}\frac{\partial k}{\partial z}\right) \tag{28d}$$

$$\frac{\partial \varepsilon}{\partial t}=\frac{\partial}{\partial x}\left(\frac{K_H}{\sigma_\varepsilon}\frac{\partial \varepsilon}{\partial x}\right)+\frac{\partial}{\partial y}\left(\frac{K_H}{\sigma_\varepsilon}\frac{\partial \varepsilon}{\partial y}\right)+\frac{\partial}{\partial z}\left(\frac{K_V}{\sigma_\varepsilon}\frac{\partial \varepsilon}{\partial z}\right) \tag{28e}$$

$$\frac{\partial S}{\partial t}=\frac{\partial}{\partial x}\left(D_H\frac{\partial S}{\partial x}\right)+\frac{\partial}{\partial y}\left(D_H\frac{\partial S}{\partial y}\right)+\frac{\partial}{\partial z}\left(D_V\frac{\partial S}{\partial z}\right) \tag{28f}$$

It is noted that the diffusion terms need to be solved separately by splitting them futher into horizontal ones and vertical ones because of the large spatial scale difference between the horizontal and vertical directions. To ensure conservation of each physical quantity on the Soroban grid, the explicit finite volume approach is used for solving the horizontal diffusion terms. Similar approaches were proposed by Slordal[15] and Stelling and van Kester[16] as a modification of the σ-level model. Take the diffusion of the quantity in the y-direction on the two-dimensional mesh (**Fig. 7**), for example. The problem is given by

$$\frac{\partial \phi}{\partial t}=\frac{\partial}{\partial y}\left(K_H\frac{\partial \phi}{\partial y}\right) \tag{29}$$

Let k be the grid point of interest and its control volume the rectangle *abcd*. Integrating the diffusion equation over the control volume of grid point k, we have

$$\phi^{n+1}=\phi^n-\frac{\Delta t}{\Delta y\cdot\Delta z}\left(F_{bc}-F_{ad}\right) \tag{30}$$

where F_{ad}, F_{bc} = total fluxes across the edges *ad* and *bc*, respectively. As shown in **Fig. 7**, the total fluxes across the edge *ad* are from/to the control volumes of grid point *kup_jdn* and *kdn_jdn*, respectively. Total flux is determined according to the average flux across each edge portion and the lengths of these edge portions. The total fluxes across the edge *bc* are from/to the control volumes of grid point *kup_jup* and *kdn_jup*, respectively. It can be calculated the same way as the fluxes across the edge *ad*.

The vertical diffusions, since the explicit scheme is strictly constrained by the time step due to the stability requirement, are solved by the implicit central difference scheme.

Step 5: Other sources step

In this step, centrifugal terms and Coriolis terms of

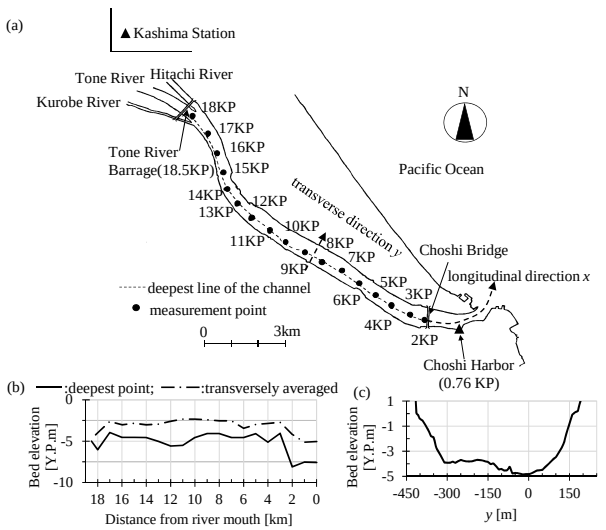

Fig. 8 Map of Tone River Estuary: (a) plan view and measurement points; (b) longitudinal profiles of bed elevation; (c) transverse profile at 14.5 KP.

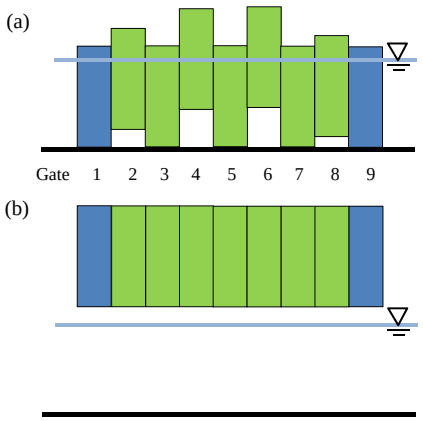

Fig. 9 Schematic of gate operations of Tone River channel: (a) gates partially opened during ordinary times; (b) gates fully opened during the flood period. Blue represents adjustment gate and green denotes slide gate.

momentum equations are included.

$$\frac{\partial u}{\partial t} = \frac{1}{R}uv + fv \tag{31a}$$

$$\frac{\partial v}{\partial t} = -\frac{1}{R}uu - fu \tag{31b}$$

Equations (31a) and (31b) are solved by the Euler explicit scheme.

Step 6: Pressure correction step

Lastly, the pressure terms of momentum equations are calculated so that the model satisfies the continuity equation.

$$\frac{\partial u}{\partial x} + \frac{\partial v}{\partial y} + \frac{\partial w}{\partial z} = 0 \tag{32a}$$

$$\frac{\partial u}{\partial t} = -\frac{1}{\rho}\frac{\partial p}{\partial x} \tag{32b}$$

$$\frac{\partial v}{\partial t} = -\frac{1}{\rho}\frac{\partial p}{\partial y} \tag{32c}$$

$$\frac{\partial w}{\partial t} = -\frac{1}{\rho}\frac{\partial p}{\partial z} - g \tag{32d}$$

By substituting equations (32b)–(32d) into the continuity equation (32a) according to the Marker and Cell (MAC) method[19], a Poisson equation for the pressure p is deduced. After the Poisson equation is solved by an incomplete LU preconditioned BiConjugate Gradient Stabilized (Bi-CGSTAB) matrix solver, the velocity components are accelerated according to equations (32b)–(32d) by the determined pressure field.

To shorten the computational time of 3-D computing, the present solver is implemented with the Message Passing Interface (MPI) library and all of the calculations mentioned above are solved in parallel. In the present study, computations have been performed by twenty CPU cores. It is found that the elapsed time can be shortened to one-tenth of non-parallel computing.

3. APPLICATION TO THE TONE RIVER ESTUARY

(1) Study site

The Tone River is the second longest river in Japan, rising in the volcanic area of the northwestern Kanto region and emptying into the Pacific Ocean. **Figure 8** shows a map of the Tone River Estuary. In the subfigures, KP represents the distance along the deepest line from the river mouth. The low water channel is approximately 600 m wide at ordinary times, while during flood periods the width can extend to 1000 m. The gradient of the river bed is almost flat (bed slope below 1/10000).

The total freshwater inflows to the Tone River Estuary are from the Hitachi River, Kurobe River and Tone River. The main freshwater input is from the Tone River. The Tone River Barrage was constructed across these three rivers at 18.5 KP, and water gates were separately installed at each river channel to control the discharge into the Tone River Estuary. Gate operation of the Hitachi and Kurobe River channels is simple. The gates are fully closed under normal conditions, and are fully opened if there is a discharge from the Hitachi River or Kurobe River. On the other hand, the gate operation of the Tone River channel is complicated and changes depending on the flow rate at upstream Fukawa Station (76.5 KP) and the salinity around the barrage. As shown in **Fig. 9**, the gates at the Tone River channel consist of two adjustment gates (double sluice gates) separately installed on both sides of the barrage and seven slide gates (single sluice gate) in the center of the barrage. As shown in **Fig. 9a,** at ordinary times, several gates

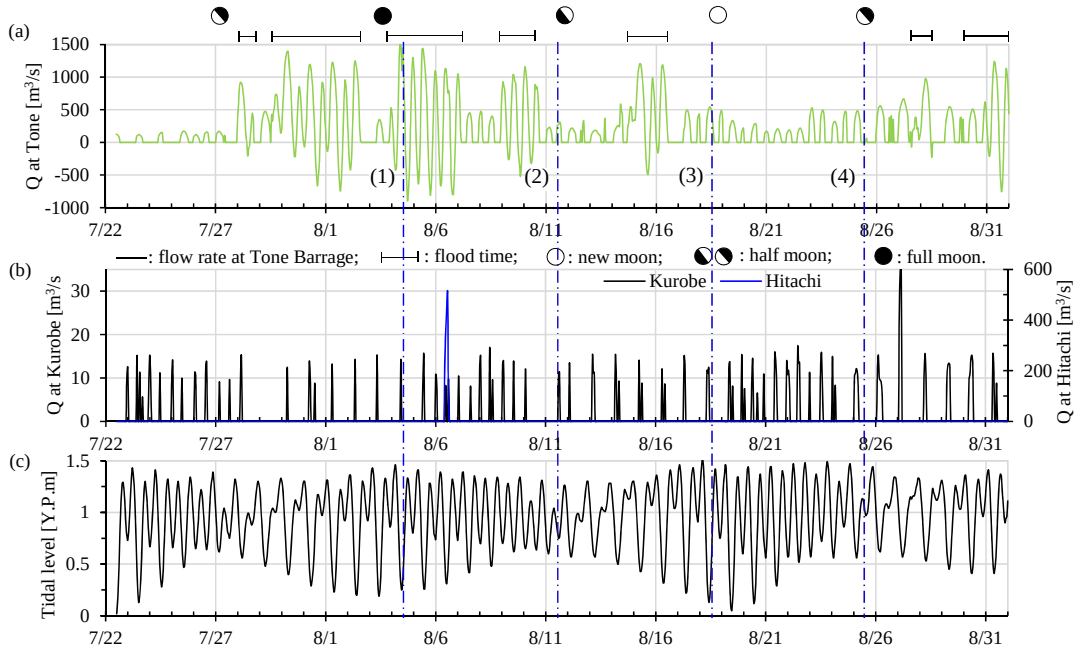

Fig. 10 Freshwater discharge, tidal level during the period from July 22 to August 31 of 1997: (a) freshwater discharge of Tone River; (b) freshwater discharge of Kurobe River (black line) and Hitachi River (blue line); (c) tidal level at Choshi Harbor.

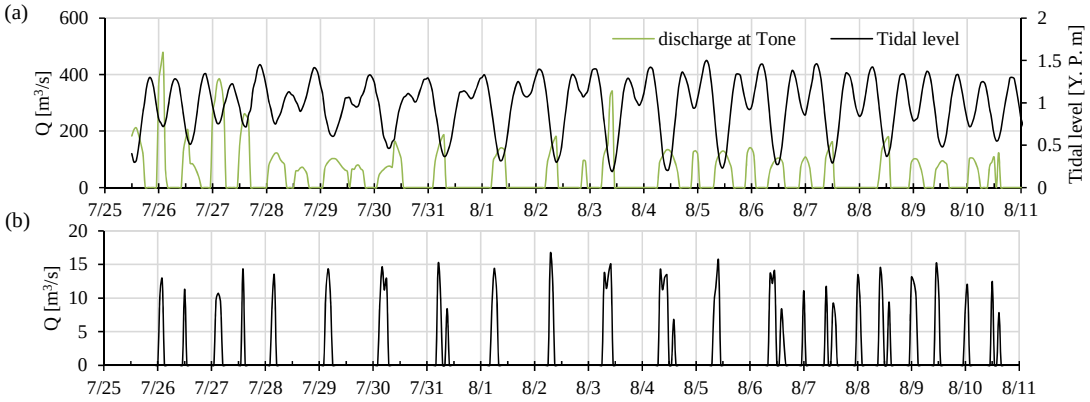

Fig. 11 Freshwater discharge, tidal level during the period from July 25 to August 11 of 2001: (a) freshwater discharge of Tone River and tidal level at Choshi Harbor; (b) freshwater discharge of Kurobe River.

are partially opened in the low-salinity period and fully closed in the high-salinity period. Conversely, all the gates will be fully opened (**Fig. 9b**) when the flow rate at Fukawa Station exceeds 250 m^3/s, which is the flood period.

(2) Model setup

The computational domain is between the Tone River Barrage and the region extending 10 km offshore into the Pacific Ocean. The topographic data used for computation is made according to the bathymetry surveyed in 2001. In the longitudinal direction, the spatial grid resolution is set as Δx = 100 m in the vicinity of the barrage and river mouth, and Δx = 200 m for the rest of the region. In the transverse direction, the grid spacing is set as Δy = 25 m. The grid spacing in the vertical direction is variable during the computation and its initial value is equally set as Δz = 0.1 m.

Extensive field measurements were conducted by Suzuki in the region between 2 KP and 18 KP for many years[2]. Two representative measurement periods are used to examine the predictive capability of the model. During the first, in August 1997, the vertical profiles of salinity along the deepest line from 2 KP to 18 KP at 1 km interval were measured weekly by Multiparameter Water Quality Meter (ACL-1183-PDK), which showed evident changes in salinity intrusion processes between spring and neap tides; along-channel current structures were collected for six rounds from 2 KP to 18 KP on August 18 using Acoustic Doppler Current Profiles (ADCP) mounted aboard a survey vessel, which showed the detailed variation of along-channel velocity in one tidal period. During the second period, in August 2001, cross-channel distributions of salinity and velocities were observed at 15.5 KP on August 4, which showed the existence of lateral flow; vertical profiles

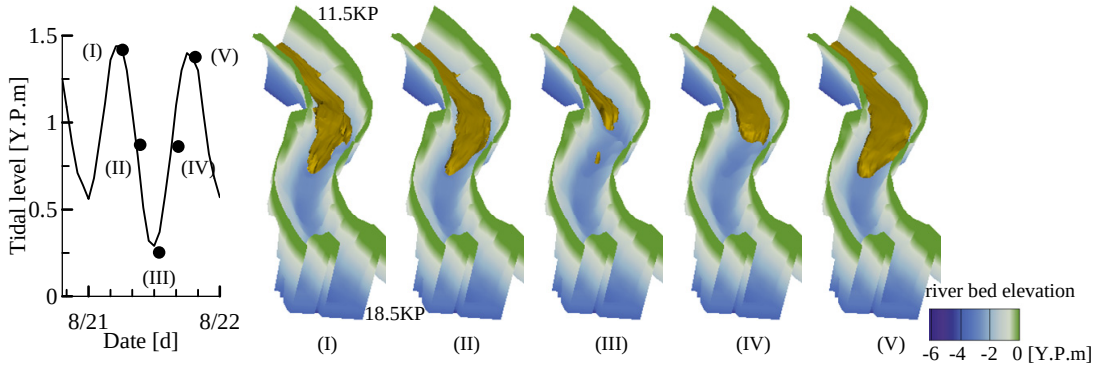

Fig. 12 Three-dimensional distributions of high-salinity water body (above 25 psu) in one tidal period.

of along-channel velocity at the deepest point of 14.5 KP were continuously measured for ten days from August 1 to 10, and showed characteristic residual flows. For simplicity, the period in August 1997 is abbreviated to "Period 1" and the period in August 2001 is abbreviated to "Period 2".

The computations for these two periods were separately initiated from July 22, 1997 and July 25, 2001 to allow sufficient time to erase impacts caused by initialization. Initial conditions for salinity and water level are given by the field data on initial days and velocities are given as zero. The upstream boundaries are set at the Tone River Barrage (18.5 KP). At the upstream boundaries, freshwater discharges are imposed separately at the Hitachi, Tone and Kurobe channels based on the actual gate operation of each channel. In the open-gate region, the velocity is defined in terms of flow rate, and salinity is specified at 0 psu. In the closed-gate region, the velocity is zero and there is no salinity flux across the upstream boundary. At the downstream boundary, the tidal level at Choshi Harbor is applied and salinity is 34 psu. **Figures 10** and **11** show the freshwater discharge from the Hitachi River, Tone River and Kurobe River, as well as the tidal level at Choshi Harbor. During Period 1, the gates at Tone channel were fully opened for flood control several times while the gates at Hitachi channel were only opened once, on August 6. During Period 2, the gates at Tone channel were partially opened when there was a discharge and the gates at Hitachi channel were kept closed.

Time series of wind data at Kashima Station (inland area about 18 km away from the Tone River Barrage) and Choshi Station (-1 KP) are applied at the water surface. Wind speeds in the region lower than -1 KP are derived from the wind data at Choshi Station and the speeds between the Tone River Barrage and -1 KP are estimated according to the interpolation of the wind data at Choshi Station and Kashima Station. The shear stress acting on the water surface is given by

$$\tau_{wind} = \rho_{air} C_D U^2 \tag{33}$$

where ρ_{air} =air density; C_D =wind drag coefficient; U = wind speed at 10 m above the water surface. Kondo's formula[20] deduced on the open ocean is used to estimate the coefficient C_D. There are still some uncertainties in formulating the wind stress because the wind stress is actually affected by the local topography, such as river banks, and wind fetch on the river is limited and shorter than that on the open ocean.

At the same time, to reveal the unique features of the 3-D model, the laterally-averaged 2-D model is also employed to simulate the same computational periods. The same computational conditions mentioned above are also used for this 2-D model's computation. As introduced above, parts of the gates in the cross-channel direction of the Tone River Barrage are partially opened from the bottom during ordinary times. The freshwater discharging from the bottom mixes with the high-salinity bottom water first and then floats onto the surface. Because the effect of this laterally-varied gate operation on the upstream boundary conditions cannot be properly considered in the 2-D model, the gates at the Tone River Barrage are assumed to be fully opened in the 2-D model.

(3) Model results in Period 1 (Aug. 1-31, 1997)

a) Dynamics of high-salinity water body

The dynamics of a high-salinity water body (above 25 psu), together with the topography in the neighborhood of the barrage from 11.5 KP to 18.5 KP and the variation in tidal level, are presented in **Fig. 12** (I)–(V) on the right-hand side. The tidal level for each moment (I)–(V) is marked on the left-hand side of the figure. The state of the high-salinity water body, i.e., retreating during ebb tide (II, III) and intruding during flood tide (IV, V) along the deepest line of the channel, is well reproduced.

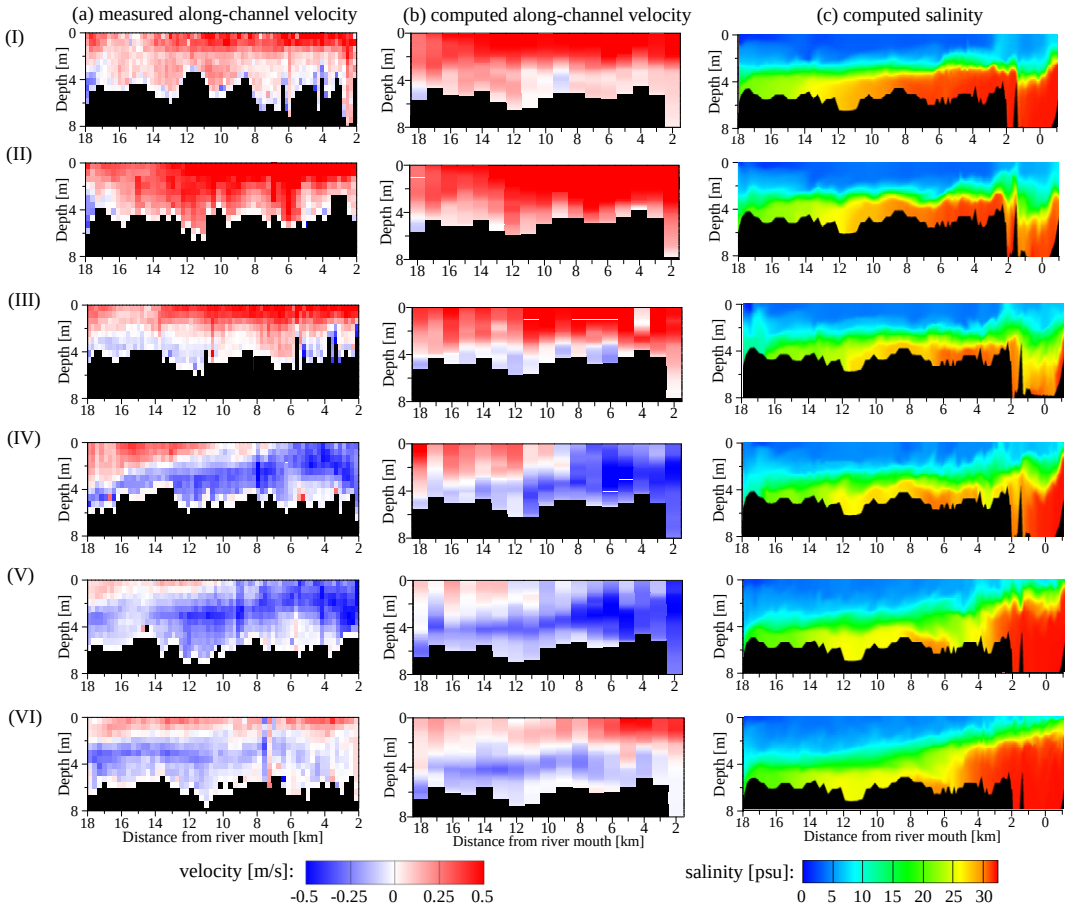

Fig. 13 Longitudinal profiles of measured (left panels) and computed (middle panels) along-channel velocity along the deepest line as well as corresponding longitudinal profiles of computed salinity (right panels) for each round on August 18. Positive (red) currents are seaward, whereas negative (blue) currents are landward.

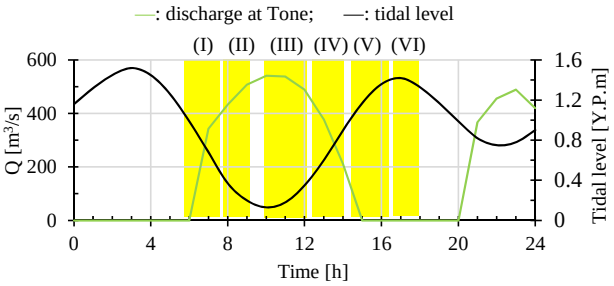

Fig. 14 Hydraulic conditions and measurement time (yellow bars) for each round on August 18.

b) Variation in velocity structures in one tidal period

In **Fig.13**, comparisons of measured (left) and computed (middle) along-channel velocity distributions from 2 KP to 18 KP along the deepest line and the corresponding computed salinity distribution (right) of each round are presented. The red color stands for seaward currents and the blue color for landward currents. **Figure 14** shows hydraulic conditions and measurement period for each round on August 18. The tidal phase during these six rounds (I–VI) ranges from the middle of ebb tide to the end of flood tide. According to the field data, at ebb tide, a weak reverse flow is generated in the vicinity of the barrage (18 KP) and seaward currents prevail in the rest of the region (I, II). Seaward currents become much stronger in the second round (II), which results in the spatial fluctuation of the fresh-saline water interface. At flood tide, landward currents first appear near the bottom in the third round (III) and the current structure changes to a "reversed" two-layer flow with landward surface and seaward bottom currents in the fourth round (IV). Variations in the velocity field as an effect of the tidal level change are reasonably reproduced by the 3-D model.

c) Salinity distributions

The contour plots of the measured and computed (3-D and 2-D) salinity along the deepest line from 2 KP to 18 KP are shown in **Fig. 15**. Plots of the vertical profiles of measured and computed salinity at several selected locations are shown in **Fig. 16**. In **Fig. 16**, the red line represents the vertical profiles of 3-D computed salinity along the deepest line and the blue square denotes the 3-D computed results averaged over the cross-channel direction. There is no large difference between the 3-D computed and laterally-averaged 3-D computed salinity. This indicates that there is no large change in salinity along the cross-channel direction.

The numbers (**Fig. 15** and **16**) on the left of the

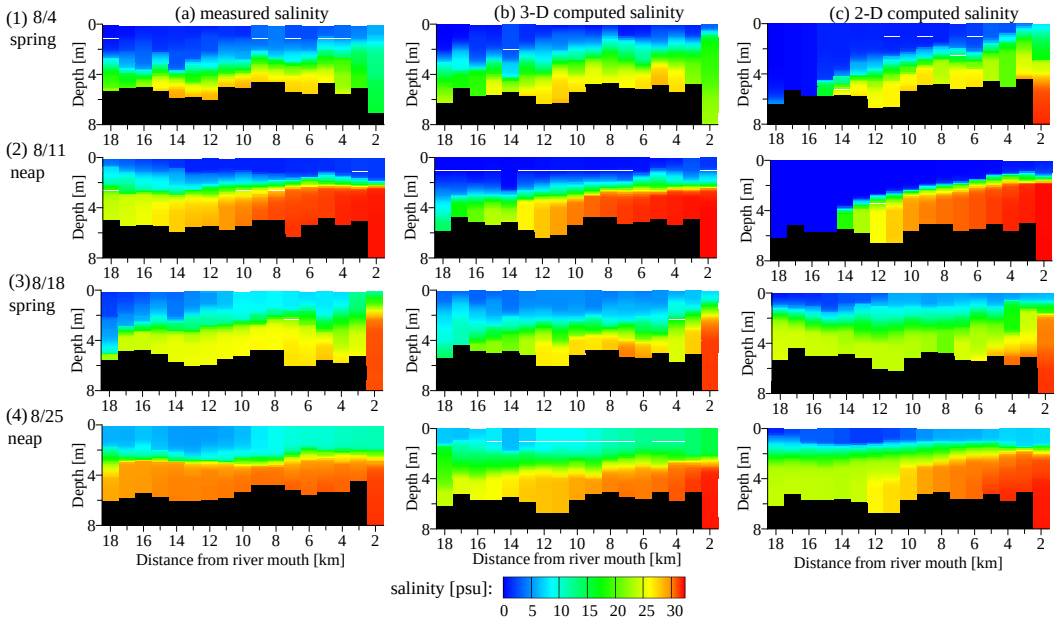

Fig. 15 Comparisons of longitudinal profiles of measured and computed (3-D and 2-D) salinity along the deepest line: (a) measured data; (b) results of 3-D salinity simulation; (c) results of 2-D salinity simulation.

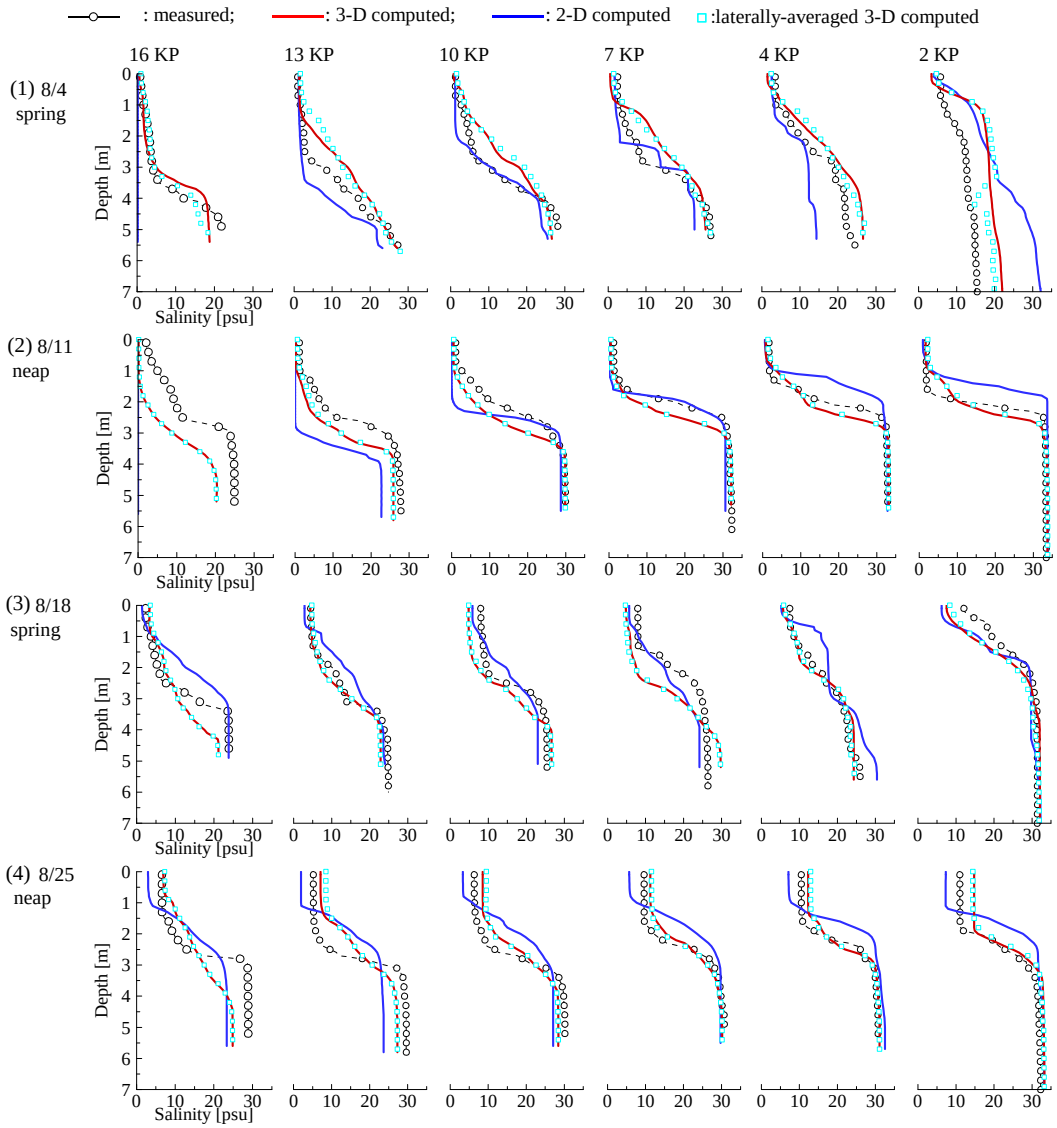

Fig. 16 Comparisons of measured and (3-D and 2-D) computed vertical salinity profiles at selected locations.

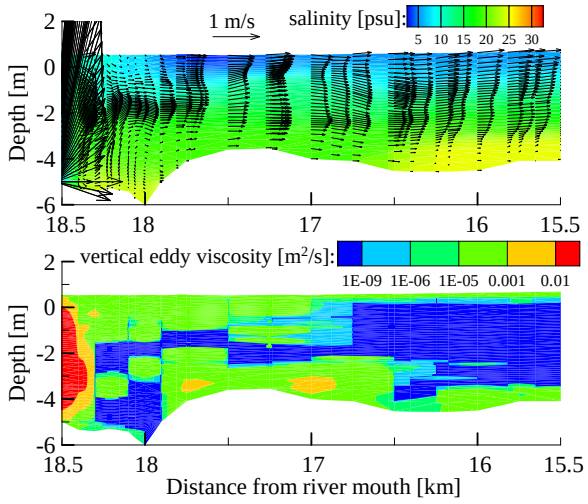

Fig. 17 Salinity, velocity vector and vertical eddy viscosity in the vicinity of the upstream boundary during discharge on August 25.

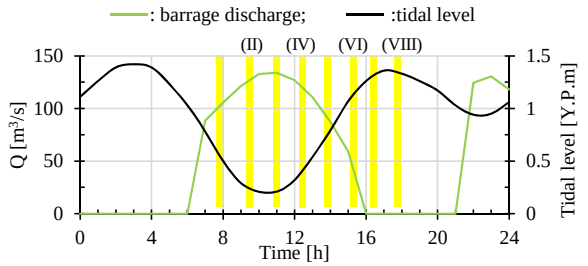

Fig. 18 Hydraulic conditions and measurement time (yellow bars) for each round on August 4, 2001.

figures correspond to the time of field measurements shown with the same numbers in **Fig. 10**. August 4 and August 18 occurred during the spring tides and August 11 and August 25 during the neap tides. According to the field data, during the neap tides, the Tone River Estuary has strong and stable salinity stratification, while during the more energetic spring tides, greater turbulence is created, resulting in more mixing in the water columns and less stratification. The computed results shown in **Fig. 15b** indicate that the 3-D model simulates the temporal variations of salinity very well, whereas the 2-D results (**Fig. 15c**) show that salinity is obviously lower than the measured data up-estuary (13 KP–18 KP). A possible reason is that the 2-D model cannot consider the gate operation's influence as properly as the 3-D model on the upstream boundary conditions. As shown in **Fig. 9**, there are nine gates installed in the Tone River channel along the cross-channel direction. **Fig. 9a** shows that only several gates are partially opened in ordinary times. Therefore, the high-salinity water in the vicinity of the closed gates would not be flushed away immediately, and it will be entrained by the freshwater from the upstream boundary and gradually transported downstream. Since the effect of a laterally-varied gate operation can be considered in the 3-D model, the declining salinity in the upper estuary changes gradually and it is close to the measured data. On the other hand, because the effect of a laterally-varied gate operation cannot be considered in the 2-D model, the gates at the Tone River Barrage are assumed to be fully opened. As a result, the salinity is uniformly flushed away and transported downstream by the freshwater discharging from the barrage without considering the difference in gate operation in the cross-channel direction. It may be the reason for the lower salinity profiles in the upper estuary in the 2-D model.

Meanwhile, the 3-D computed salinity on August 25 is not reproduced as reasonably as those on other days. As shown in **Fig. 10**, there is a discharge from the Tone River right before the measurement time on August 25 and the peak value is approximately 500 m^3/s. **Figure 17** shows that the vertical mixing is much stronger and the direction of velocity heads upwards near the upstream boundary during this discharge, which leads to more saline water in the lower layer entrained into the upper layer and transported downstream by the estuarine circulation. Actually it can be estimated that the vertical mixing in the vicinity of the barrage should be strong. This may be the major reason for the relatively low degree of reproducibility of 3-D computed salinity on August 25. It is thus necessary to conduct further studies, such as on employing a relatively fine grid resolution in the vicinity of the barrage hereafter. However, both 3-D and 2-D computed results reasonably reproduce the temporal variation of vertical salinity stratification due to spring and neap tidal cycles.

(4) Model results in Period 2 (Aug. 1–10, 2001)

a) Transverse distributions of salinity and velocity at 15.5 KP

Eight rounds of transverse measurements at 15.5 KP related to salinity, along-channel velocity and cross-channel velocity were conducted on August 4, 2001. **Figure 18** gives the hydraulic conditions and measurement time for each round. The tidal phase in the measurement period is from the middle of ebb tide to the end of flood tide. The transverse structures of measured salinity, along-channel velocity and cross-channel velocity are shown in **Fig. 19**. The corresponding computed results in the Tone River Estuary transect are represented by the hydrodynamic model as well (**Fig. 20**).

As revealed in **Fig. 19b**, in the second round (II), seaward currents prevail in the surface layer, and landward currents have already appeared near the bottom. In the fourth (IV) and sixth (VI) rounds, seaward currents still exist in the surface layer but shrink greatly, and the bottom layer is dominated by landward currents. River discharge from the Tone

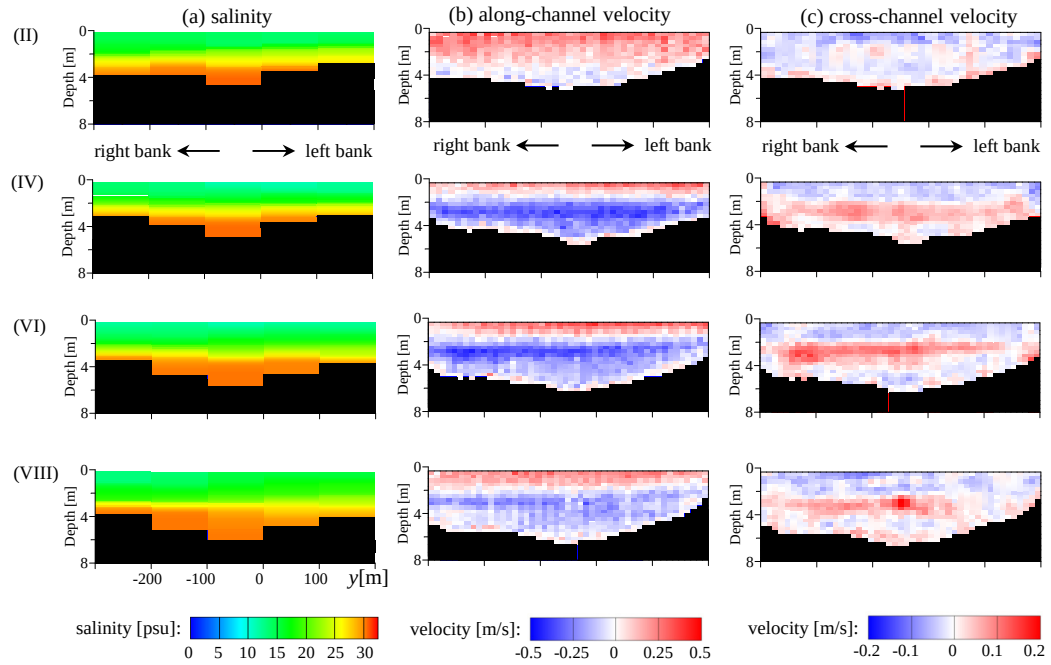

Fig. 19 Transverse profiles of measured data at 15.5 KP: (a) salinity; (b) along-channel velocity. Positive (red) currents are seaward (looking landward), whereas negative (blue) currents are landward; (c) cross-channel velocity. Positive (red) currents represent currents towards the left bank looking landward, whereas negative (blue) currents are currents to the right bank.

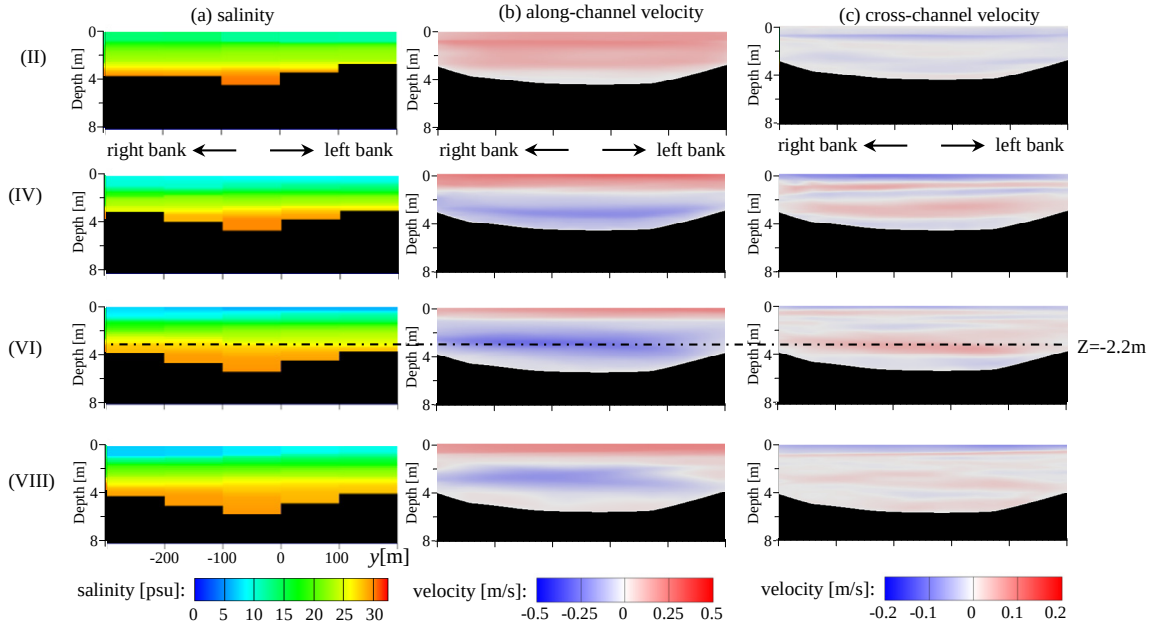

Fig. 20 Transverse profiles of computed results at 15.5 KP: (a) salinity; (b) along-channel velocity. Positive (red) currents are seaward (looking landward), whereas negative (blue) currents are landward; (c) cross-channel velocity. Positive (red) currents represent currents towards the left bank looking landward, whereas negative (blue) currents are currents to the right bank.

River contributes to the seaward currents in the surface layer. As shown in **Fig. 19**(VI), the magnitudes of landward currents feature relatively large values around the interface of fresh-saline water layers and a clockwise lateral flow is generated in the bottom layer. As shown in **Fig. 8**, the Tone River Estuary slightly meanders around 15.5 KP. Therefore, as shown in **Fig. 19a**, in the sixth round(VI), more saline water is clearly seen on the right bank (outer bank) and less saline water on the left bank (inner bank), probably due to the centrifugal force. This salinity difference generates the baroclinic pressure gradient in the cross-channel direction. In consequence, the currents towards the left bank around the halocline and the clockwise flows in the saline bottom water layer are generated. **Figure 20** shows that the transverse distributions of salinity and velocities and their temporal variations are simulated well by the model. Vector plots of computed horizontal and lateral flow fields during the measurement

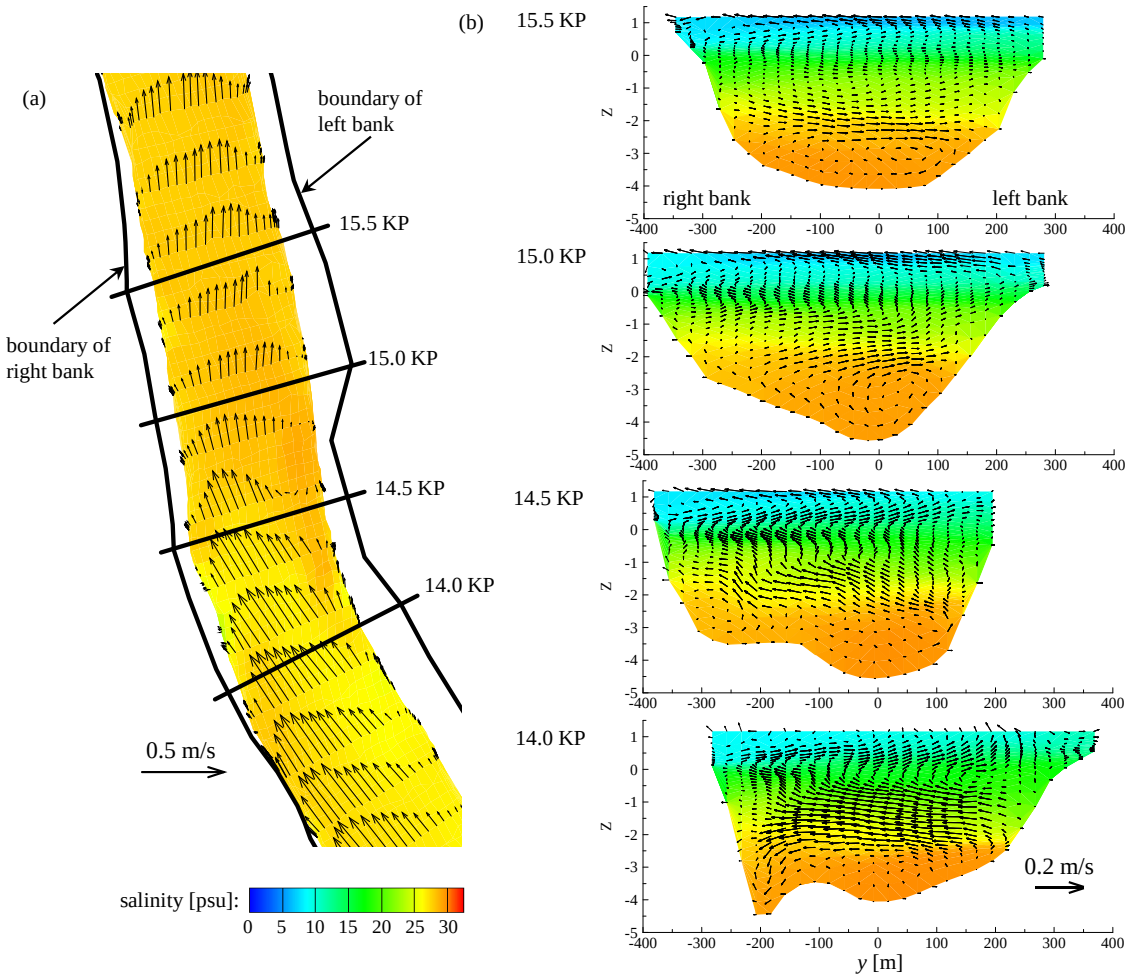

Fig. 21 Vector plots of computed horizontal and lateral flow fields. Contour shows salinity: (a) horizontal circulation at Z = -2.2 m, where halocline is located; (b) transverse profiles of currents (v, w) and salinity.

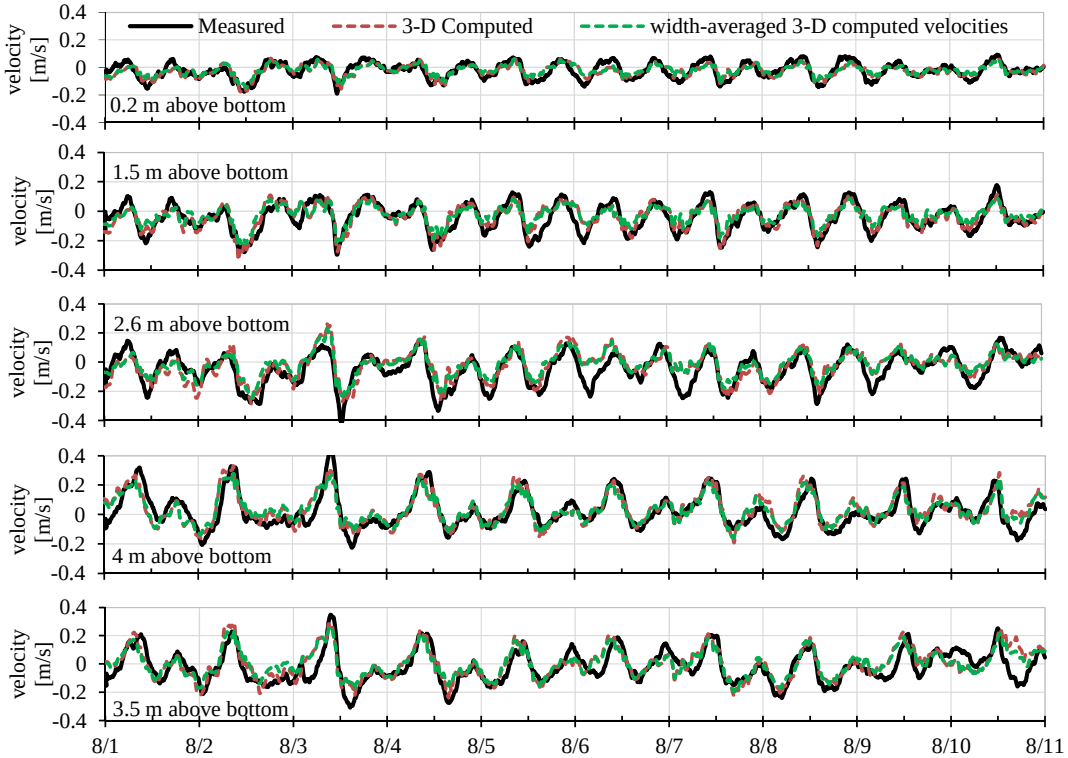

Fig. 22 Time-series plots of measured velocities (black lines), 3-D computed velocities (dashed red lines) and width-averaged 3-D computed velocities (dashed green lines) at 14.5 KP, August 2001.

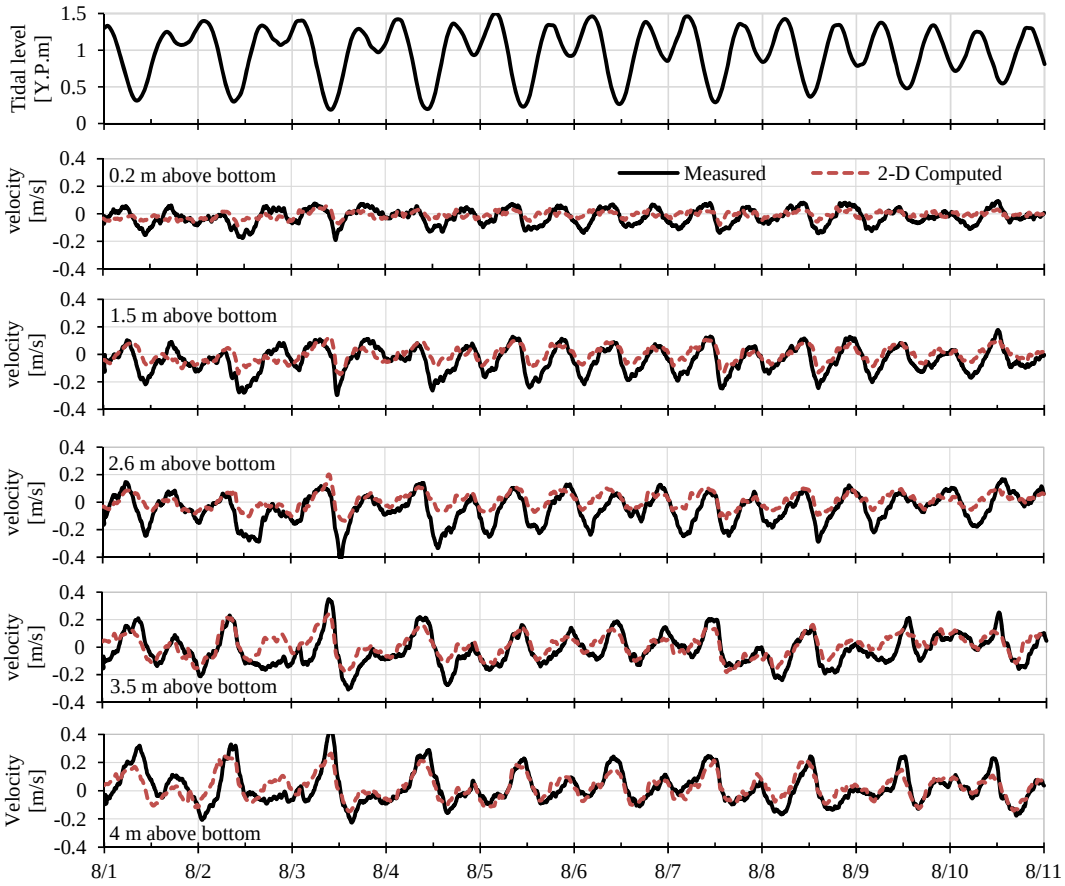

Fig. 23 Time-series plots of measured velocities (black lines) and 2-D computed velocities (dashed red lines) at 14.5 KP, August 2001.

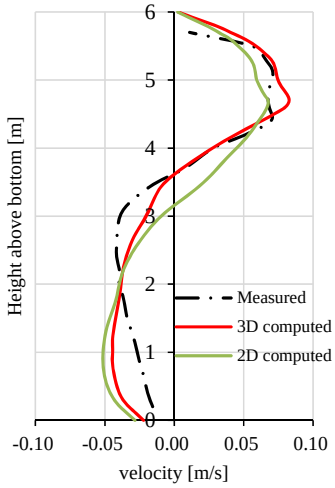

Fig. 24 Comparison between measured and computed (2-D and 3-D) resident flow averaged over ten days at 14.5 KP.

time of the sixth round are presented in **Fig. 21**. Lateral flows are obviously generated in the cross-sections of the river's meandering region. It is suggested that the present model has the capability of reproducing the currents in the river channel with small meandering. Differences between the measurements and the model predictions exist as well. The computed along-channel velocity (**Fig. 20b**) and cross-channel velocity (**Fig. 20c**) are smaller than the measured value (**Fig. 19b** and **c**). As mentioned in the previous section, for Period 1, the salinity stratification has a tendency to become weak in the upper estuary in the computed results. The computed results shown in **Fig. 20** indicate that, during Period 2, the computed salinity stratification is also weaker than the measured one. As a result, the effect of the baroclinic pressure gradient becomes small. This is considered to be the reason for the under-estimation of along-channel velocity and cross-channel velocity at the cross-section of 15.5 KP.

b) Time-series of along-channel velocity of each depth and residual flow

The residual velocity field helps in understanding the long-term water exchange inside the estuary. For this reason, the residual flow for a ten-day period is computed. **Figure 22** shows the time-series plots of measured and 3-D computed along-channel velocities of several depths at 14.5 KP. The dashed red line is the 3-D computed velocities and the dashed green line the 3-D computed velocities averaged over the cross-channel direction. There is no large change in along-channel velocities along the cross-channel direction. These results quantitatively agree well with the measured data, which indicates that the model has the capability to predict the along-channel

velocities at 14.5 KP in response to the change in tidal level. **Figure 23** shows the comparison of measured and 2-D computed along-channel velocities. Although the reverse flows are slightly weaker than the measured data during flood tide, the variation in velocities is also reasonably reproduced by the 2-D simulation. The comparisons of computed (2-D and 3-D) and measured estuarine circulation averaged over ten days are shown in **Fig. 24**. To a certain extent, the reproducibility of the 3-D model is better than the 2-D model. It is verified that the 3-D model has the capability to predict the estuarine circulation process.

4. DISSOLVED OXYGEN TRANSPORT IN TONE RIVER ESTUARY

Dissolved oxygen (DO) is one of the most important indexes of water quality. In the Tone River Estuary, the decomposition of organic matter at the bottom and in the water column is the major cause of oxygen depletion. After the construction of barrage, the regular movement of the salt wedge makes salinity stratification more stable which correspondingly reduces the supply of DO from the oxygen-rich surface layer to the oxygen-insufficient bottom layer. Hypoxia often occurs at the head of the salt wedge, which depends not only on the oxygen consumption rate but also the rate of oxygen supply from the river mouth[2]. In this section, to advance the understanding of the mechanism of DO transport in the Tone River Estuary, a DO transport model is incorporated into the hydrodynamic model.

(1) Advection-diffusion equation for dissolved oxygen

The DO transport process can be mathematically described by advection and diffusion terms as follows:

$$\frac{DC}{Dt} = \frac{\partial}{\partial x}\left(D_{H,C}\frac{\partial C}{\partial x}\right) + \frac{\partial}{\partial y}\left(D_{H,C}\frac{\partial C}{\partial y}\right) + \frac{\partial}{\partial z}\left(D_{V,C}\frac{\partial C}{\partial z}\right) + S_{DO} \quad (34)$$

$$D_{H,C} = \frac{K_H}{\sigma_c},\ D_{V,C} = \frac{K_V}{\sigma_c} \quad (35)$$

where C = DO concentration; $D_{H,C}$, $D_{V,C}$ = diffusion coefficients of DO in horizontal and vertical directions, respectively; S_{DO} = source and sink terms; σ_c = turbulent Schmidt number of DO (= 1.0).

(2) Source and sink terms

Terms such as those representing the flux of oxygen through the water surface and bottom, and biochemical oxygen demand in the water column are introduced as source and sink terms in equation (34).

The boundary condition at the water surface is specified by expressing the net transfer of oxygen to water through the interface between the atmosphere and the water column in terms of the surface reaeration process, that is,

$$\rho K_V \frac{\partial C}{\partial z} = -K_r\left(DO_s - C_s\right) \quad (36)$$

where K_r = reaeration coefficient; DO_s = saturated oxygen concentration at the water surface; and C_s = actual oxygen concentration at the water surface. The value of K_r is referred to in the study by Suzuki et al.[21] concerning hypoxic dynamics in the Tone River Estuary, where $K_r = 3.0\times10^{-5}$ m/s. The saturated oxygen concentration DO_s here is temperature T and salinity S dependent and given by the American Public Health Association (APHA)[22] (1985):

$$\ln DO_s = -139.34411 + \frac{1.575701\times10^5}{T} - \frac{6.642308\times10^7}{T^2} + \frac{1.2438\times10^{10}}{T^3} - \frac{9.621949\times10^{11}}{T^4} - \frac{S\times10^{-2}}{1.80655}\left(3.1929 - \frac{1.9428\times10^3}{T} + \frac{3.8673\times10^5}{T^2}\right) \quad (37)$$

The depletion of oxygen from the water column overlying the bottom sediment is primarily caused by the decomposition of organic matter in the sediments. The boundary condition at the bottom is given by the DO net flux through the interface of the water column and the bottom sediment owing to sediment oxygen demand (SOD), that is,

$$\rho K_V \frac{\partial C}{\partial z} = -K_{sed}\cdot C_b \quad (38)$$

where K_{sed} = deoxygenation coefficient (per unit area) and C_b = actual oxygen concentration at the bottom.

Biochemical oxygen demand in the water can be formulated as

$$S_{SOD} = -\left(\frac{C}{C + DO_0}\right)\cdot\Delta k \quad (39)$$

where DO_0 = half-saturation constant of DO (= 0.5 mg/l) and Δk = oxygen consumption rate.

Deoxygenation coefficient K_{sed} and oxygen consumption rate Δk are site-specific parameters. To quantify the value of deoxygenation coefficient K_{sed}, the bottom sediment was sampled at the deepest points of 5, 9 and 18 KP by Ishikawa et al.[2]. Water in the salt wedge was also sampled 50 cm above the bed at the deepest points of 6, 11 and 16 KP. According to the lab experiment, the deoxygenation coefficient K_{sed} is 0.17 mg per day (per unit area) and the oxygen consumption rate Δk is approximately 0.6 mg/l per

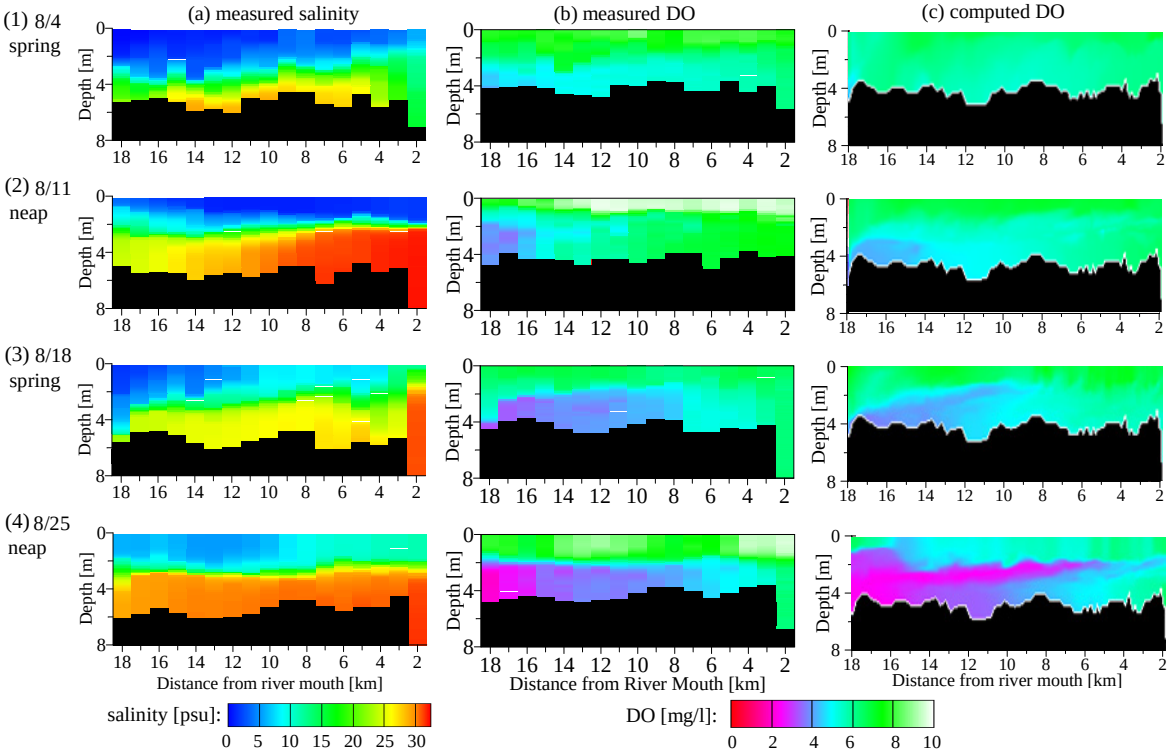

Fig.25 Measured longitudinal profiles of salinity (left panels) and DO (middle panels) on each measurement day and their corresponding computed DO results (right panels).

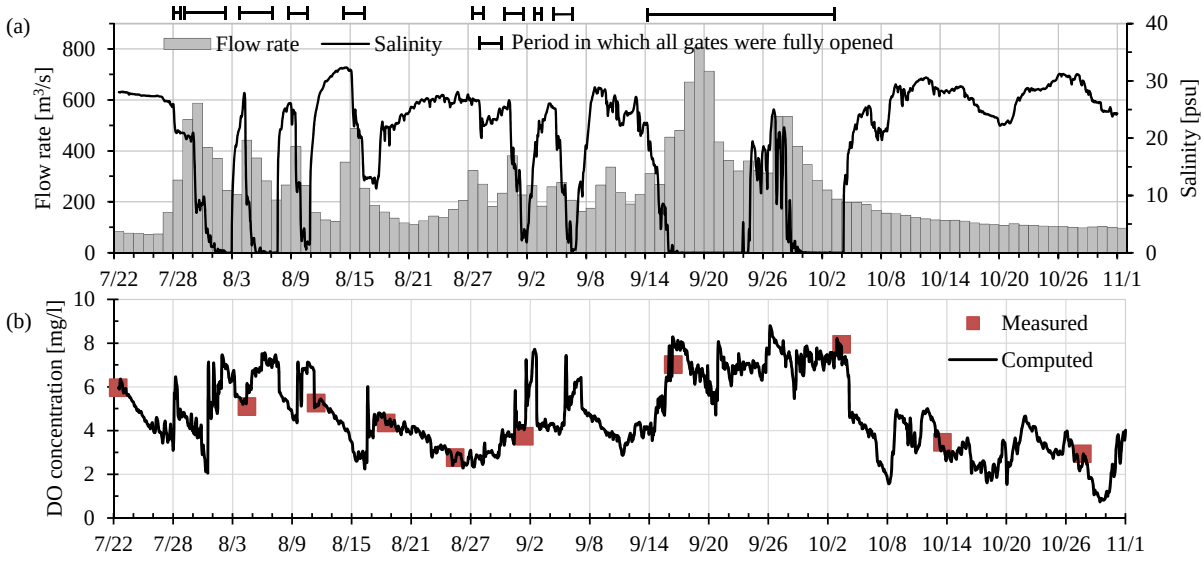

Fig. 26 Long-term variation of dissolved oxygen at 1 m above the bottom of 16 KP: (a) average daily flow rate at Fukawa Station (76.5KP) and salinity near river bed at 16.5 KP; (b) dissolved oxygen concentration at 1 m above the bottom of 16 KP.

day[2)].

Since there are no available measured data to determine the amount of DO going into the computational domain at upstream and downstream boundaries, saturated boundaries are specified according to equation (37).

(3) DO transport in Tone River Estuary

A long-term simulation of approximately 100 days from July 22 to October 31, 1997 was performed to model the onset and development of hypoxia at the head of the salt wedge.

a) Spatial and temporal variation in DO

Figure 25 gives the comparisons between computed and measured DO concentrations along the deepest line from 2 KP to 18 KP, as well as the corresponding measured salinity distributions on the measurement days. As shown in **Fig. 25a**, during the spring tides, the salinity stratification becomes weaker since the increase in horizontal shear stress

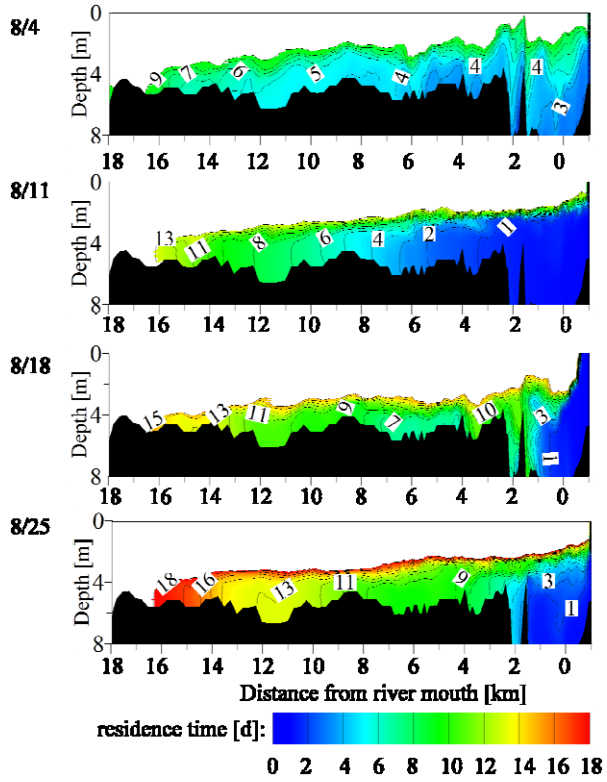

Fig.27 Residence time of seawater.

enhances vertical mixing, whereas during the neap tides, the salt wedge intrudes deeply and the salinity stratification becomes stronger, thus more high-salinity water is transported upstream. In the measured results of DO, the hypoxic water body first appears on August 11 at the head of the salt wedge and then expands downstream untill August 18. Hypoxia becomes worse on August 25. One major reason is that the salinity stratification is stronger on that day and little oxygen can be transported from the oxygen-rich upper layer to the bottom layer. The pattern of DO concentration change at the head of the salt wedge captured by the field data are reasonably reproduced by the computed results. However, there is an obvious difference between the computed and measured DO on August 25. It is because the computed salinity stratification in the upper estuary is weaker than it actually should be on August 25 (**Fig. 15**), which leads to more low-oxygen water transported into the surface layer.

b) Long-term variability of DO at the head of the salt wedge

According to previous field measurements[22], the anaerobic condition was often formed at the head of the salt wedge and the center of the low-oxygen water usually stayed around 16 KP. Therefore, the long-term variability of DO near the bottom at 16 KP is studied. **Figure 26** presents the time series of DO concentration at 1 m above the bottom of 16 KP. **Figure 26a** shows the flow rate at Fukawa Station (76.5 KP); the black line is the salinity near the river bed at 16.5 KP. As described in section 3.1, when the flow rate at Fukawa Station exceeds 250 m^3/s, the gates are fully opened. As the gates are fully opened, the saline water at 16 KP is flushed away and it will soon return to normal after the flood. **Figure 26b** shows the DO concentration at 1 m above the bottom of 16 KP. Measured data show that a large drop in DO concentration occurs twice during these three months: one is in the middle of August and the other is in October. The computation correctly reproduces the time series of DO in the whole three months, including these two events. At the same time, the trend of DO concentration at 16 KP has a correlation with the variation in salinity at 16.5 KP. When the gates are fully opened, the bottom salinity at 16.5 KP is flushed away and the DO concentration increases because DO at 16.5 KP is supplied by the oxygen-rich freshwater from the river discharge. When the gates are partially opened or completely closed, the DO concentration at 16.5 KP continues to decline.

c) Residence time of seawater

Residence times of seawater give an estimate of how quickly the water body exchanges its volume of "aged water" in the estuary with the "new water" from the river mouth. They are provided as a first-order evaluation of estuarine water quality. Lower residence times generally correspond to higher water quality. Additionally, the residence time of seawater gives an indication of when the hypoxic water body may occur in the bottom layer and how the situation goes on.

To determine the residence time, a trace scheme shown in Ishikawa et al.[2] is utilized. Residence times of seawater in the Tone River Estuary are computed by performing a dyerelease study in such a manner that its concentration at the river mouth is equal to the "date of release". The concentration of the dye substance enables us to estimate the age of seawater in the salt wedge. **Figure 27** shows the computed residence time of seawater; the low-salinity surface water layer is left blank. On August 11, the hypoxia occurs at the head of the salt wedge, which indicates that a span of 13 days can be considered as the time for the onset of the hypoxia. On August 18, the residence time of seawater is 15 days, which leads to the expansion of hypoxia. The residence time at the river mouth becomes discontinuous because vertical mixing is very strong during the spring tide on August 18. On August 25, with the prolongation of the residence time of seawater to up-estuary, the hypoxic water body grows and expands toward the river mouth. Results of the residence time of seawater

indicate that the rate of oxygen supply from the river mouth is another major factor of the onset and development of hypoxia.

5. CONCLUSIONS

A three-dimensional CIP-Soroban flow solver has been developed to predict the salinity field and velocity structure in stratified estuaries. To study the performance of this flow model, we numerically computed the time-dependent, three-dimensional salinity field and velocity structure in the Tone River Estuary for two periods. The computed results not only confirmed the model's capability to reproduce the salinity and velocity field but also gave new insights into the physical processes involved in the circulation and mixing in the Tone River Estuary. Temporal and spatial variations in salinity brought about by the spring and neap tide effects were simulated reasonably well by the 3-D model. The lateral flows at 15.5 KP during the flood tide due to the curvature of the channel were also well reproduced. The results of a long-term DO simulation of 100 days showed good agreement with the field data. The intensity of the density stratification and residence time of seawater are considered to be the two major factors controlling the onset and development of hypoxia.

REFERENCES

1) Valle-Levinson, A.: *Contemporary issues in estuarine physics*, Cambridge University Press, p. 12, 2010.
2) Ishikawa, T., Suzuki, T. and Qian, X.: Hydraulic study of the onset of hypoxia in the Tone River Estuary, *J. Environ. Eng.*, Vol. 130, pp. 551-561, 2004.
3) Kobayashi, Y., Sasaki, T., Ishikawa, T. and Minoura, Y.: Seasonal variation of bottom sediment characteristics in the Tone River Estuary, *Ann. J. Hydraul. Eng., JSCE*, Vol. 54, pp. 679-684, 2010.
4) Kurup, R. G., Hamilton, D. P. and Phillips, R. L.: Comparison of two 2-dimensional laterally averaged hydrodynamic model applications to the Swan River Estuary, *Math. Comp. in Simul.*, Vol. 51, pp. 627-638, 2000.
5) Bloss, S., Lehfeldt, R. and Patterson, J.: Modeling turbulent transport in stratified estuary, *J. Hydraul. Eng.*, Vol. 114, pp. 1115-1133, 1988.
6) Nakamura, T., Kojima, T. and Ishikawa, T.: CIP-Soroban method for two-dimensional estuary flow with a river width and free water surface, *Ann. J. Hydraul. Eng., JSCE*, Vol. 50, pp. 805-810, 2006.
7) Cheng, R. T.: Numerical models of wind driven circulation in lakes, *Appl. Math. Model.*, Vol. 1, pp. 141-158, 1976.
8) King, I. P.: Strategies for finite element modeling of three-dimensional hydrodynamic systems, *Adv. Wat. Res.*, Vol. 8, pp. 69-76, 1985.
9) Wang, Q., Daniov, S. and Schroter, J.: Comparison of overflow simulations on different vertical grids using the Finite Element Ocean circulation Model, *Ocean Model.*, Vol. 20, pp. 313-335, 2008.
10) Yabe, T. and Aoki, T.: A universal solver for hyperbolic-equations by cubic-polynomial interpolation, I. One-dimensional solver, *Comput. Phys. Commun.*, Vol. 66, pp. 219-232, 1991.
11) Yabe, T., Ishikawa, T., Wang, P. Y., Aoki, T., Kadota, Y. and Ikeda, F.: A universal solver for hyperbolic-equations by cubic-polynomial interpolation, II Two-and three-dimensional solvers, *Comput. Phys. Commun.*, Vol. 66, pp. 233-242, 1991.
12) Yabe, T., Xiao, F. and Utsumi, T.: The constrained interpolation profile method for multiphase analysis, *J. Comput. Phys*., Vol. 169, pp. 556-593, 2001.
13) Yabe, T., Mizoe, H., Takizawa, K., Moriki, H., Im, H. N. and Ogata, Y.: Higher-order schemes with CIP method and adaptive Soroban grid towards mesh-free scheme, *J. Comput. Phys.*, Vol. 194, pp. 57-77, 2004.
14) Takizawa, K., Yabe, T., Tsuguawa, Y., Tezduyar, T. and Mizoe, H.: Computation of free-surface flows and fluid-object interactions with the CIP method based on adaptive meshless Soroban grids, *Comput. Mech.*, Vol. 41, pp. 8091-8099, 2006.
15) Slordal, L. H.: The pressure gradient force in sigma-co-ordinate ocean models, *Int. J. Numer. Methods in Fluids*, Vol. 24, pp.987-1017, 1997.
16) Stelling, G. S. and van Kester, J. A. Th. M.: On the approximation of horizontal gradients in sigma co-ordinates for bathmetry with steep bottom slope, *Int. J. Numer. Methods in Fluids*, Vol. 18, pp.915-935, 1994.
17) UNESCO: The Practical salinity scale 1978 and the international equation of state of seawater 1980, *Technical Papers in Marine Science 36*, p. 25, 1981.
18) Smagorinsky, J.: General circulation experiments with the primitive equations, Part I: the basic experiment, *Monthly Weather Review*, Vol. 91, pp. 99-152, 1963.
19) Harlow, F. H. and Welch, J. E.: Numerical calculation of time-dependent viscous incompressible flow of fluid with a free surface, *Phys. Fluids*, Vol.8, pp.2182-2189, 1965.
20) Kondo, J.: Air-sea bulk transfer coefficients in diabatic conditions, *Boundary-Layer Meteor.*, Vol. 9, pp. 91-112, 1975.
21) Suzuki, T., Ishikawa, T. and Yokoyama, K.: Field measurement and numerical simulation of estuarine circulation in a river estuary, *Proceeding of River Engineering*, Vol. 9, pp. 259-264, 2003.
22) American Public Health Association (APHA): Standard methods for the examination of water and wastewater, APHA, Washington, D. C., 1985.

(Received September 5, 2012)